Soil Dynamics and Earthquake Engineering 43 (2012) 139–159

Contents lists available at SciVerse ScienceDirect

Soil Dynamics and Earthquake Engineering

journal homepage: www.elsevier.com/locate/soildyn

Time-domain forward and inverse modeling of lossy soils with frequency-independent Q for near-surface applications

D. Assimaki [a], L.F. Kallivokas [b,*], J.W. Kang [c], W. Li [a], S. Kucukcoban [b]

[a] School of Civil and Environmental Engineering, Georgia Institute of Technology, Atlanta, GA 30332, USA
[b] Department of Civil, Architectural and Environmental Engineering, The University of Texas at Austin, Austin, TX 78712, USA
[c] Department of Civil Engineering, New Mexico State University, Las Cruces, NM 88003, USA

ARTICLE INFO

Article history:
Received 26 September 2010
Received in revised form
3 July 2012
Accepted 3 July 2012

ABSTRACT

In this paper, we are concerned with a full-waveform-based methodology that allows the simultaneous imaging of the soil's stiffness and attenuating properties, using solely the soil's surficial response to probing waves.

To date, field observations of small-strain wave attenuation in geomaterials at moderate spatial scales suggest that a commonly used metric of intrinsic and apparent attenuation, the seismic quality factor Q, is frequency-independent for a wide part of the frequency spectrum, including the frequency range of interest to seismic applications. We discuss first the forward simulation of waves in near-surface soil deposits directly in the time-domain using simplified models that adequately approximate nearly frequency-independent Q. To this end, we first review various attenuation models that aim at reproducing the frequency-independent Q behavior, and conclude, supported by site analyses, that, even though a generalized Maxwell body with eight Maxwell elements in parallel (GMB8) provides the best fit to frequency-independent Q, we favor a version of it with fewer parameters (GMB2), in order to reduce modeling complexity, while still retaining good agreement with the GMB8 model.

We report on forward site analyses that lend credence to the choice of the GMB2 simplified model. We, then, use the GMB2 constitutive relation in the context of full-waveform inversion, and report on numerical experiments that lead to the imaging of the soil's properties in heterogeneous semi-infinite domains.

1. Introduction

Attenuation phenomena in cyclic, vibratory and dynamic problems involving the soil refer to one or more of the following mechanisms: (i) *radiation* attenuation or damping due to outward wavefront expansion from the source (geometric spreading); (ii) *apparent* attenuation, namely phenomenological decay of the propagating energy due, primarily, to scattering effects that result in energy redistribution; and (iii) *intrinsic* attenuation due to energy dissipation mechanisms in the material itself.

Intrinsic attenuation refers collectively to all the mechanisms that convert energy into heat. For example, at the microscopic level, friction at the grain boundaries and along thin cracks is a primary mechanism of intrinsic attenuation. Experiments have also revealed that fluid flow losses due to the relative movement between the solid and fluid phases play also a role, albeit secondary, in intrinsic attenuation. Squirting phenomena, partial saturation effects, and geometric effects (e.g., scattering by small pores and irregularities, selective reflection from thin beds, etc.) are among other mechanisms also contributing to intrinsic attenuation [1]. By contrast to these microscopic sources of attenuation, macroscopic mechanisms contributing to attenuation include the reflection and transmission of waves at material interfaces as well as wave scattering in heterogeneous media: attenuation due to all macroscopic contributors is referred to as *apparent* attenuation. Thus, while intrinsic attenuation removes energy from the system, radiation and apparent attenuation redistribute the wave energy within the medium. In seismology, the term *attenuation* is typically used to refer to the combined effects of intrinsic *and* apparent attenuation, that is, to the total attenuation propagating waves experience, excluding radiation damping.

To accurately model propagating waves within the Earth for applications ranging from seismic hazard assessment to geotechnical site characterization and geophysical probing, all the aforementioned forms of attenuation need to be accounted for. Of all attenuation forms, to date, modeling radiation damping in heterogeneous domains, while still an open problem, is probably the one

* Corresponding author.
E-mail addresses: dominic@gatech.edu (D. Assimaki), loukas@mail.utexas.edu (L.F. Kallivokas), jwkang@nmsu.edu (J.W. Kang), wli3@gatech.edu (W. Li), ksezgin@mail.utexas.edu (S. Kucukcoban).

0267-7261/$ - see front matter © 2012 Elsevier Ltd. All rights reserved.
http://dx.doi.org/10.1016/j.soildyn.2012.07.001

approached and understood the best: continuum models and associated numerical approaches that properly account for radiation conditions at truncation surfaces have been developed for direct time-domain simulations and are being continually refined. By contrast, continuum models that account for either the combined effects of intrinsic and apparent attenuation or models that decouple their effects, are, in general, scant, and even scantier in the time-domain. Whereas partial differential equations (PDEs) describing wave motion in elastic heterogeneous media in the time-domain are known for centuries (Navier equations), equations accounting for attenuation in a manner consistent with observations are hard to construct. More importantly, even when, for certain models, the time-domain PDEs can be obtained, their numerical solution is expensive; even worse, when such models are used to guide inversion, the inversion becomes computationally intractable.

The source of the difficulty is multifold: (i) typical measures of attenuation are based on observations of energy decay, and may be overly simplistic as betrayed by the four most commonly used metrics, which include the *damping ratio* ξ, the *logarithmic decrement* δ, the *attenuation factor* α, and the *quality factor* Q (or dissipation or attenuation factor Q^{-1}). All metrics, either directly or indirectly, imply a form of frequency dependence that may or may not be representative of physical behavior. (ii) Incorporation of the above metrics into a constitutive relation implies the adoption of a viscoelastic model with a complex modulus: the modulus is typically expressed as a function of the attenuation metric. Subsequent use of the constitutive relation to arrive at a governing PDE for the modeling of wave motion in an attenuating medium is straightforward only in the frequency-domain. For example, even if the attenuation metric is frequency-independent, the resulting complex modulus is usually frequency-dependent, thus leading, upon inversion of the constitutive relation in the time-domain, to a PDE that could, for example, include convolutional terms making it onerous for applications. (iii) Even when the physics of the problem (e.g. wave motion at moderate length scales) suggest that the attenuation metrics could be approximated as frequency-independent, simplified models are often multi-parametric, which, in turn, presents two difficulties: firstly, ascription of physically consistent numerical values to the parameters requires guidance by physical experiments, which are often not in tune with the models. And secondly, the inverse problem associated with such a large number of spatially distributed parameters (>2) becomes computationally intractable, if not impossible.

Owing to these difficulties, it appears that, at the moment, the problem of constructing a PDE in the time-domain that will adequately account for all attenuation effects is eluding definitive conclusion. Thus, here too we focus only on a partial solution, motivated primarily by the interest to invert for attenuation metrics of near-surface soil deposits: to accomplish this, it is paramount that the number of model parameters be kept to a minimum. In general, it is accepted (and supported by field observations) that at large spatial scales, apparent (scattering) attenuation dominates over intrinsic, while also exhibiting frequency-dependent behavior. On the other hand, at moderate scales, intrinsic attenuation is dominant, and, in fact, the associated quality factor Q appears to be frequency-independent [2]. Thus, of key interest here is to arrive at a model involving a few parameters that could represent adequately a frequency-independent Q over the frequency range of interest to seismic and geotechnical site characterization applications in direct time-domain simulations.

Simultaneous inversion for both elastic (stiffness, velocity, slowness, etc.) and attenuating properties in the time-domain remains an open problem with very few attempts reported in the literature. A notable exception is the work of Askan et al. [3] where, however, the authors linked Q to the velocity (stiffness), and thus, effectively, reduced the problem to a single (spatially distributed) parameter. In what we report here, we attempt to simultaneously invert for both stiffness and Q, both of which could vary arbitrarily in space.

In Sections 2 through 4 of the remainder of this paper we first discuss and compare soil attenuation models; specifically: in Section 2 we review commonly used attenuation metrics, and connect the metrics to observations, focusing mostly on the quality factor Q; in Section 3 we repeat the basic relations for the quality factor Q in the context of viscoelasticity; and in Section 4 we review extensively attenuation models relying on Q. In Section 5, we discuss *forward* site analyses that provide sufficient support for the choice of a particular order generalized Maxwell body as adequately representing soil attenuation for a range of frequencies of practical interest. In Section 6, we discuss a full waveform-based inversion methodology, which, based solely on surface records in the time domain, reconstructs the site's velocity (stiffness) and Q profiles, both of which are spatially distributed. We summarize our conclusions in Section 7.

2. Attenuation metrics and observations

In geotechnical engineering, the parameter traditionally used as a measure of energy dissipation during harmonic excitation is the *material damping ratio* ξ, defined as

$$\xi = \frac{1}{4\pi}\frac{\Delta W}{W}, \tag{1}$$

where ΔW is the amount of energy dissipated in a cycle of harmonic excitation within a certain material volume, while W is the peak elastic energy (W) stored in the system within the same volume (Fig. 1). The resonant column test (RC), based on one-dimensional wave propagation theory, is, possibly, the most widely employed technique to measure the material damping ratio ξ in the laboratory [4]. In RC tests, the damping ratio is determined from the half-power bandwidth method in forced-vibration mode, or via the logarithmic decrement method when the specimen is in free vibration mode (Fig. 1) [5,6]. The logarithmic decrement δ is given in terms of ξ as

$$\delta = \frac{2\pi\xi}{\sqrt{1-\xi^2}}. \tag{2}$$

Another often used parameter is the *spatial attenuation* α, used to express the exponential decay of the response envelope under one-dimensional harmonic assumptions; α is related to the logarithmic decrement δ by

$$\alpha = \frac{\delta\omega}{2\pi c_P}, \tag{3}$$

where ω denotes the circular frequency, and c_P the phase velocity. By far though, seismic attenuation is commonly characterized by the *quality factor* Q, a term adopted from the electrical circuit theory [7]. This dimensionless parameter is defined, similarly to the damping ratio, as the ratio of the amount of energy dissipated (ΔW) over the peak elastic energy (W) stored in the system:

$$Q = \frac{2\pi W}{\Delta W}. \tag{4}$$

In homogeneous, non-dispersive, media all four attenuation metrics are related. In particular, the first three can be expressed in terms of the quality factor (or its reciprocal, the dissipation factor Q^{-1}) as

$$\xi = \frac{1}{2Q}, \quad \delta = \frac{\pi}{Q}, \quad \alpha = \frac{\omega}{2c_P Q}. \tag{5}$$

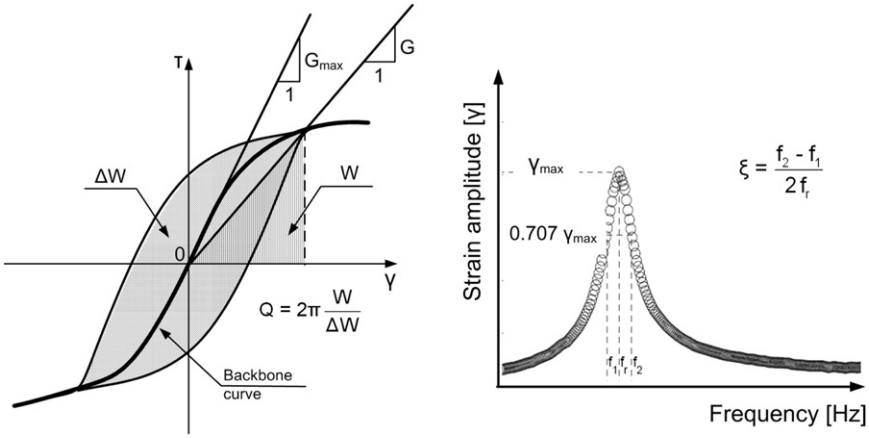

Fig. 1. Cyclic stress–strain curve; peak stored energy (W) and dissipated energy (ΔW) over a cycle of loading (left); damping ratio ξ evaluation using the halfpower bandwidth method (right).

Published laboratory and field experimental studies show that intrinsic attenuation is practically frequency-independent, at least up to moderately high frequencies. This indicates that the mechanisms resulting to energy absorption of elastic wave energy in solids are not of the same nature as in fluids, where the attenuation factor has been shown to vary as the square of frequency. Based on observations of seismic attenuation in the crust, models were initially developed to explain observations of frequency-independent Q at low frequencies (<1 Hz). Early review papers that discuss proposed mechanisms for intrinsic absorption that lead to frequency-independent Q^{-1} include [7–9].

In rock mechanics, the majority of the proposed intrinsic attenuation models are based on relaxation mechanisms, which have characteristic times that depend on the physical dimensions of the elements in the rock. This characteristic time leads to values of Q^{-1} that peak at some frequency and decrease rapidly away from that value. Assuming that rocks are composed of elements spanning a wide range of dimensions, superposition of multiple relaxation peaks can lead to frequency-independent attenuation over some frequency range. Note that for seismic waves to remain causal when attenuation is simulated, the assumption of frequency-independent Q^{-1} needs to be accompanied by frequency-dependent amplitude and phase [10].

For softer geomaterials such as sands, clays, silts and gravel, several studies have been published in the recent years describing the dependency of soil damping ratio at small strains on loading frequency. Among others, one can mention the work by Iwasaki et al [11], Isenhower [12], Tatsuoka and Shibuya [13], Kim et al. [14], Fioravante et al. [15], Porovic and Jardine [16], Tatsuoka et al. [17,18], d'Onofrio et al. [19,20], Di Benedetto and Tatsuoka [21], and Vucetic and Tabata [22].

For cohesionless soils in particular, published data show that there is little frequency effect on the dynamic properties of sand. Hardin and Black [23] found that shear modulus of dry sands is essentially independent of frequency from low, quasi-static frequencies to hundreds of Hertz. Iwasaki et al. [11] performed torsional shear and resonant column tests on dry and saturated sands and did not observe any appreciable shear modulus variation between the two tests at frequencies of 0.1 Hz and about 100 Hz, respectively. Bolton and Wilson [24] studied the soil properties of a dry sand at medium to large strain amplitude with a torsional shear test at 1 mHz and a resonant column test at 45–95 Hz. No obvious variation of dynamic properties with respect to frequency was found, particularly at lower strain amplitudes. More recently, Kim [25] also observed nearly constant soil properties for dry sand from torsional shear and resonant tests. Wang and Santamarina [26] showed that the frequency-independent small-strain damping in dry granural media is of non-frictional nature. Instead, thermoelastic loss was suggested to account for small-strain energy loss in air-dry soils. In summary, similar to hard rocks described above, the small-strain damping of clean sands and gravels has been shown to be practically insensitive to changes in the strain rate [2].

Unlike sands, however, the dynamic properties of clayey soils (i.e., clays and coarse-grained soils with significant clay content) often demonstrate frequency effects, with material damping ratio shown to be much more dependent on frequency than the small-strain shear modulus is (G_{max}) [20,27–32]. To date, the time-dependent nature of dynamic properties in cohesive soils is not very well understood. Many studies have indicated a modest increase in shear modulus of approximately 4% per decade of frequency on clayey subgrades [25], kaolin [27], sandy lean clay and fat clay [6], and stiff Italian clays [20] in the frequency range of 1 mHz to about 200 Hz. With a silty clayey sand, Lerouil and Marques [33] also found a modest shear modulus increase at frequencies less than 1 Hz, but a larger 30% increase per decade frequency in the range of 10–100 Hz. Focusing on the effects of frequency on the damping ratio of clayey soils, published data generally indicate that damping ratio increases with increasing frequency above about 10 Hz. Several soils also exhibit increases in damping ratio with decreasing frequency at frequencies less than about 0.1 Hz. Shibuya et al. [27] explained the above findings by considering that at very high frequencies the effects of viscosity dominate, while at very low frequencies, creep effects govern the dynamic response of soils. He proposed a schematic diagram comprising three frequency regions (Phases A-C), to characterize the variation of damping ratio with frequency (Fig. 2). As can be readily seen, seismic ground motion loading frequencies ($\approx 0.5-10$ Hz) almost exclusively belong in Phase B, and therefore for earthquake engineering applications, intrinsic attenuation may be assumed as frequency independent for cohesive soils as well.

3. Attenuation and dispersion in linear viscoelasticity

The small-strain response of geomaterials is often modeled using classical viscoelasticity, whereby the stress is proportional to both strain and strain rate; under one-dimensional assumptions, the constitutive relation can be cast as [10]

$$\hat{\sigma}(\omega) = M(\omega)\hat{\epsilon}(\omega), \tag{6}$$

where σ and ϵ refer to the stress and strain, respectively, that arise when a plane wave propagates with a frequency ω (and a complex wavenumber k^*) in a homogeneous viscoelastic medium characterized by the complex modulus $M(\omega)$. A caret in (6)

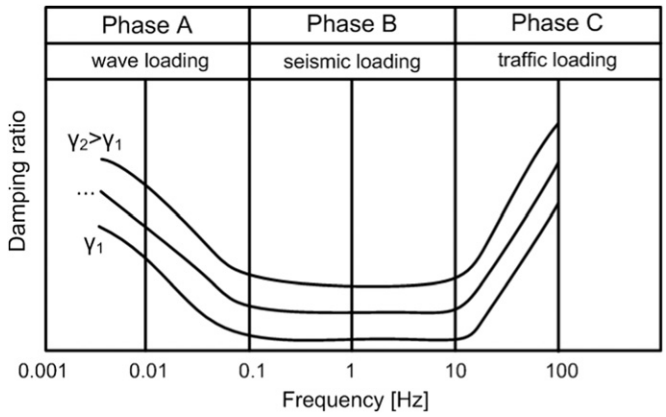

Fig. 2. Frequency dependency of intrinsic attenuation for cohesive geomaterials (modified from [27]): (i) Phase A ($f<0.1$ Hz), material damping due to creep; (ii) Phase B ($0.1<f<10$ Hz), material damping hysteretic in nature and independent of frequency; and (iii) Phase C ($f>10$ Hz), material damping viscous in nature.

implies Fourier-transform of the subtended quantity. The definition also implies that

$$M=\rho c^{*2}(\omega),\quad k^*(\omega)=\frac{\omega}{c^*(\omega)}=\frac{\omega}{c_P(\omega)}+i\alpha(\omega), \tag{7}$$

where c^* denotes complex velocity, and ρ material density. Moreover, the following limits establish the early- and long-time behavior of the modulus, respectively:

$$m_U=\lim_{\omega\to\infty}M(\omega),\quad m_R=\lim_{\omega\to 0}M(\omega), \tag{8}$$

where m_U denotes the *unrelaxed* modulus that expresses the proportionality between stress and strain as soon as the stress is applied and before the material has started to relax via creeping, and m_R denotes the *relaxed* modulus. Thus, in the context of viscoelasticity, the quality factor is defined as (Krönig [34])

$$Q(\omega)=\frac{\Re eM(\omega)}{\Im mM(\omega)}, \tag{9}$$

or, using (7)

$$Q(\omega)=\frac{\omega}{2\alpha(\omega)c_P(\omega)}-\frac{\alpha(\omega)c_P(\omega)}{2\omega}. \tag{10}$$

Clearly, Q is, by definition, frequency-dependent. Specific expressions for Q depend on the particular forms for the attenuation α and the phase velocity c_P one chooses in order to represent a specific material behavior. We discuss next various models proposed for modeling Q in geomaterials, and discuss implications of their adoption in time-domain formulations of wave propagation. As discussed in Section 2, a frequency-independent modeling of Q seems to be well supported by field observations, and, therefore the focus is on models that can capture, as best as possible, a nearly frequency-independent Q behavior.

4. Attenuation models for viscoelastic geomaterials

We review two broader classes of models: firstly, we discuss seismic attenuation models that are typically applicable only in the frequency-domain given the complexity of the frequency dependence of the expressions for the quality factor Q; and secondly, assemblies of springs and dashpots, which, while resulting in simpler $Q-\omega$ dependence, lack the ability to model (nearly) frequency-independent Q. However, extensions of these simpler models to the generalized rheological model assemblies provide reasonable modeling of frequency-independent Q behavior: these are reviewed last in Section 4.3.

4.1. Seismic attenuation models

The summarized attenuation models are:

1. Kolsky model [35].
2. Modified Kolsky model [36].
3. Futterman model [37].
4. Strick–Azimi model [38].
5. Kjartansson's constant Q model [39].
6. Azimi's second and third models [40].
7. Müller's power-law Q model [41].
8. The Cole–Cole model [42].

Kolsky [35] investigated the propagation of short mechanical pulses in viscoelastic solids. It was experimentally shown that the high-frequency components travel faster and are attenuated more rapidly than the lower-frequency components. It was also demonstrated that the pulse shape can be recovered from frequency-dependent modulus and damping. However, the model he proposed was not causal. Futterman [37] focused on the dispersion and used the Kramers–Krönig expressions to relate the dispersive part to the absorptive part. Azimi et al. [40] looked analytically into the relation between the attenuation law and phase velocity for three almost-linear absorption laws and one almost-quadratic absorption law. In [35,37,40], all the authors treated the quality factor as being nearly constant (or weakly frequency-dependent) in a limited frequency range of interest. Kjartansson [39] presented a linear model for attenuation in which Q is exactly independent of frequency in the whole frequency range. This constant Q model is completely defined by Q and the phase velocity at an arbitrary reference frequency. By following a different procedure, namely applying the Kramers–Krönig relations to the viscoelastic modulus, Müller [41] studied the attenuation-dispersion relation with $Q\sim\omega^\gamma$. Thus, the author was able to obtain high- and low-frequency approximations (and also exact results when $\gamma=1/m$, $m=1,2,\ldots$) for the viscoelastic modulus. The author in [41] also investigated the case $\gamma=0$ and recovered Kjartansson's [39] constant Q model.

More recently, Wang and Guo [36] proposed a modification for the basic Kolsky model so that it satisfies the Kramers–Krönig relation. They also compared eight earth models, i.e., the modified Kolsky model, Strick–Azimi model, Kjartansson's model, Azimi's second and third models, Müller's model, Zener model (SLS), the Cole–Cole model, and a new general linear model.

For each of the attenuation models described below, we provide the attenuation factor, phase velocity, and quality factor expressions[1]:

1. Kolsky model [35]:

$$\alpha(\omega)=\frac{\omega}{2c_rQ_r},\ \frac{1}{c_P(\omega)}=\frac{1}{c_r(\omega)}\left(1-\frac{1}{\pi Q_r}\ln\frac{\omega}{\omega_r}\right),$$
$$Q(\omega)\simeq Q_r-\frac{1}{\pi}\ln\frac{\omega}{\omega_r}. \tag{11}$$

2. Modified Kolsky model [36]:

$$\alpha(\omega)=\frac{\omega}{2c_rQ_r},$$
$$\frac{1}{c_P(\omega)}=\frac{1}{c_r(\omega)}\left(1-\frac{1}{\pi Q_r}\ln\frac{\omega}{\omega_h}\right),$$
$$Q(\omega)\simeq Q_r-\frac{1}{\pi}\ln\frac{\omega}{\omega_h}, \tag{12}$$

where ω_h is about 1000π.

[1] Subscript r refers to values of reference quantities.

3. Futterman model; three different models were proposed [37]:
   - 1st model:

$$\alpha(\omega)=\frac{1}{2c_0Q_0}\begin{cases}0, & 0\le\omega\le\omega_0,\\ \omega, & \omega_0\le\omega,\end{cases}$$
$$\frac{1}{c_P(\omega)}=\frac{1}{c_0}-\frac{1}{2\pi c_0Q_0}\ln\left|\left(\frac{\omega}{\omega_0}\right)^2-1\right|, \tag{13}$$

   - 2nd model:

$$\alpha(\omega)=\frac{1}{2c_0Q_0}\begin{cases}\frac{\omega^2}{\omega_0}, & 0\le\omega\le\omega_0,\\ \omega, & \omega_0\le\omega,\end{cases}$$
$$\frac{1}{c_P(\omega)}=\frac{1}{c_0}-\frac{1}{2\pi c_0Q_0}\times\left(\ln\left|1-\left(\frac{\omega}{\omega_0}\right)^2\right|-\frac{\omega}{\omega_0}\ln\left|\frac{1-\frac{\omega}{\omega_0}}{1+\frac{\omega}{\omega_0}}\right|\right), \tag{14}$$

   - 3rd model:

$$\alpha(\omega)=\frac{\omega}{2c_0Q_0}(1-e^{-\omega/\omega_0}),$$
$$\frac{1}{c_P(\omega)}=\frac{1}{c_0}-\frac{1}{\pi c_0Q_0}\left\{\ln\left(\gamma\frac{\omega}{\omega_0}\right)-\frac{1}{2}\left[e^{-\omega/\omega_0}\overline{Ei}\left(\frac{\omega}{\omega_0}\right)+e^{\omega/\omega_0}Ei\left(-\frac{\omega}{\omega_0}\right)\right]\right\}. \tag{15}$$

   where ω_0 is a cutoff frequency, c_0 is the phase velocity at ω_0, $Q_0(\omega)=\omega/2\alpha c$, c is the non-dispersive limit of phase velocity, γ is the Euler constant, and Ei denotes exponential integral.

4. Strick–Azimi model [38]:

$$\alpha(\omega)=a_1|\omega|^{1-\beta},\quad 0<\beta<1,$$
$$\frac{1}{c_p(\omega)}=\frac{1}{c_\infty}+a_1|\omega|^{-\beta}\cot\left(\frac{\pi}{2}\beta\right),$$
$$Q(\omega)\approx\frac{|\omega|^\beta}{2a_1c_\infty}+\frac{1}{2}\cot\left(\frac{\pi}{2}\beta\right). \tag{16}$$

5. Kjartansson's constant Q model [39]:

$$\alpha(\omega)=a_1|\omega|^{1-\beta},$$
$$\frac{1}{c_p(\omega)}=a_1|\omega|^{-\beta}\cot\left(\frac{\pi}{2}\beta\right),$$
$$Q(\omega)\approx\frac{1}{2}\cot\left(\frac{\pi}{2}\beta\right)\approx\cot(\pi\beta). \tag{17}$$

6. Azimi's second and third models [40]:
   - 2nd model:

$$\alpha(\omega)=\frac{a_2\omega}{1+a_3\omega},$$
$$\frac{1}{c_p(\omega)}=\frac{1}{c_\infty}-\frac{2a_2}{\pi}\frac{\ln(a_3\omega)}{1-a_3^2\omega^2},$$
$$Q(\omega)\approx\frac{1+a_3\omega}{2a_2c_\infty}-\frac{\ln(a_3\omega)}{\pi(1-a_3\omega)}. \tag{18}$$

   - 3rd model:

$$\alpha(\omega)=\frac{a_4\omega}{1+a_5\sqrt{\omega}},$$
$$\frac{1}{c_p(\omega)}=\frac{1}{c_\infty}+\frac{a_4a_5\sqrt{\omega}}{1+a_5^2\omega}-\frac{2a_4}{\pi}\frac{\ln(a_5^2\omega)}{1-a_5^4\omega^2},$$
$$Q(\omega)\approx(1+a_5\sqrt{\omega})\left(\frac{1}{2a_4c_\infty}+\frac{a_5\sqrt{\omega}}{2(1+a_5^2\omega)}-\frac{\ln(a_5^2\omega)}{\pi(1-a_5^4\omega^2)}\right), \tag{19}$$

   where $c_\infty=\lim_{\omega\to\infty}c_P(\omega)$.

7. Müller's power-law Q model [41]:
   For $Q\gg1$,

$$Q(\omega)=Q_r\left(\frac{\omega}{\omega_r}\right)^\beta,\quad -1<\beta<1,$$
$$\alpha(\omega)=\frac{\omega}{2c_rQ_r}\left(\frac{\omega_r}{\omega}\right)^\beta,$$
$$\frac{1}{c_p(\omega)}=\frac{1}{c_r}\exp\left\{\frac{\cot\left(\frac{\pi}{2}\beta\right)}{2Q_r}\left[\left(\frac{\omega_r}{\omega}\right)^\beta-1\right]\right\}. \tag{20}$$

8. The Cole–Cole model [42]:

$$\alpha(\omega)\approx\frac{\beta|\omega\tau_c|^{1+\beta}\sin\left(\frac{\pi}{2}\beta\right)}{c_0Q_c\tau_c\left[1+|\omega\tau_c|^{2\beta}+2|\omega\tau_c|^\beta\cos\left(\frac{\pi}{2}\beta\right)\right]},$$
$$\frac{1}{c_p(\omega)}\approx\frac{1}{c_0}\left(1-\frac{\beta t\omega\tau_c|^\beta\left[\cos\left(\frac{\pi}{2}\beta\right)+|\omega\tau_c|^\beta\right]}{Q_c\left[1+|\omega\tau_c|^{2\beta}+2|\omega\tau_c|^\beta\cos\left(\frac{\pi}{2}\beta\right)\right]}\right). \tag{21}$$

Incorporation of any of the above Q expressions in the constitutive relation (6) using (9) would result, upon inversion in the time-domain (if the latter is at all possible) in a computationally cumbersome form.

4.2. Simple rheological models

Rheological models for viscoelastic materials comprise combinations of springs and dashpots in series and in parallel. Among them, the most widely employed are the Maxwell (M) model [43], the Kelvin–Voigt (KV) model [44], the Standard Linear Solid (SLS) [45], and the Maxwell–Rayleigh (MR) model [46] shown in Fig. 3.

The constitutive laws associated with each model can be cast as

$$\text{M}:\quad \sigma+\frac{\eta}{E}\dot{\sigma}=\eta\dot{\epsilon}, \tag{22}$$

$$\text{KV}:\quad \sigma=E\left(\epsilon+\frac{\eta}{E}\dot{\epsilon}\right), \tag{23}$$

$$\text{SLS}:\quad \sigma+\frac{\eta}{E+E^*}\dot{\sigma}=\left(\frac{1}{E}+\frac{1}{E^*}\right)^{-1}\left(\epsilon+\frac{\eta}{E^*}\dot{\epsilon}\right), \tag{24}$$

$$\text{MR}:\quad \sigma+\frac{\eta}{E}\dot{\sigma}=(\eta+\eta^*)\dot{\epsilon}+\frac{\eta\eta^*}{E}\ddot{\epsilon}, \tag{25}$$

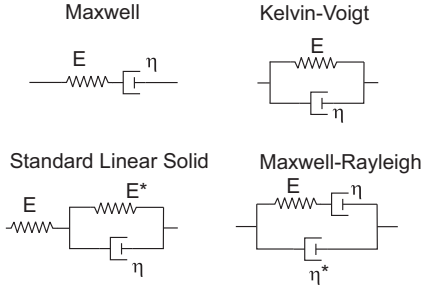

Fig. 3. Classical rheological models for viscoelastic wave propagation in geomaterials, where E, E^* denote moduli, and η and η^* denote viscous damping coefficients.

in which a dot $(\cdot)$ denotes time derivative of the subtended quantity. The complex modulus of the four rheological models is, therefore, described by the following expressions:

$$\text{M}: \quad M_{\text{M}}(\omega) = \frac{i\omega E\eta}{E+i\omega\eta}, \tag{26}$$

$$\text{KV}: \quad M_{\text{KV}}(\omega) = E+i\omega\eta, \tag{27}$$

$$\text{SLS}: \quad M_{\text{SLS}}(\omega) = \frac{E(E^*+i\omega\eta)}{E+E^*+i\omega\eta}, \tag{28}$$

$$\text{MR}: \quad M_{\text{RM}}(\omega) = \frac{i\omega E\eta}{E+i\omega\eta} + i\omega\eta^*. \tag{29}$$

Using, next, the definition of quality factor Q given by Eq. (9), the dissipation factor Q^{-1} for the simple rheological models shown in Fig. 3 becomes

$$\text{M}: \quad Q_{\text{M}}^{-1}(\omega) = \frac{E}{\omega\eta}, \tag{30}$$

$$\text{KV}: \quad Q_{\text{KV}}^{-1}(\omega) = \frac{\omega\eta}{E}, \tag{31}$$

$$\text{SLS}: \quad Q_{\text{SLS}}^{-1}(\omega) = \frac{\omega\eta E}{E^*(E+E^*)+\omega^2\eta^2}, \tag{32}$$

$$\text{MR}: \quad Q_{\text{MR}}^{-1}(\omega) = \frac{E(\eta+\eta^*)}{\omega\eta^2} + \frac{\omega\eta^*}{E}. \tag{33}$$

As shown in Fig. 4, each of the rheological models described above exhibits a different attenuation frequency-dependency. More specifically, the Maxwell and Maxwell–Rayleigh models exhibit infinite attenuation at zero frequency, and do not experience instantaneous elasticity. The Standard Linear Solid and Maxwell–Rayleigh models show a band-cut and band-pass effects, respectively. Moreover, even though the expressions for the quality factor are significantly simpler when compared with the models described in the preceding section, it is clear from Fig. 4 that they cannot readily be used to model nearly frequency-independent behavior.

4.3. Generalized nearly constant-Q rheological models

It is possible to develop more complex viscoelastic models with more realistic variations of the attenuation function Q^{-1}, using assemblies of the simple rheological models of the preceding section. The idea was originally suggested by Liu et al. [47]

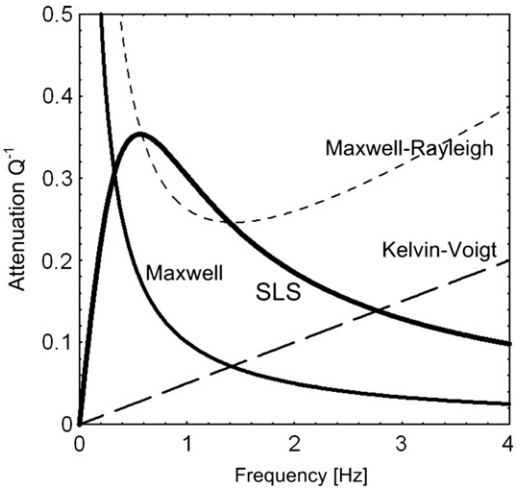

Fig. 4. Attenuation expressions of the classical rheological models shown in Fig. 3.

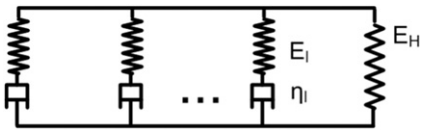

Fig. 5. Generalized Maxwell body (GMB) [54].

who used a superposition of several relaxation mechanisms to approximate the observations of *nearly constant* intrinsic Q in the crust. Since then, many attenuation models have been developed for implementation in numerical analyses of wave propagation problems based on the concept of memory variables [48,49,46,50].

The formulation of the generalized attenuation models is based on the differential form of the convolutory stress–strain relation. Considering the frequency-dependent modulus $M(\omega)$ as a rational function of the form:

$$M(\omega) = \frac{P_m(i\omega)}{R_n(i\omega)} = \frac{\sum_{l=1}^{m} p_l(i\omega)^l}{\sum_{l=1}^{n} r_l(i\omega)^l}, \tag{34}$$

and applying the inverse Fourier transform to the stress–strain relationship (6), there results

$$\sum_{l=1}^{n} r_l \frac{d^l\sigma(t)}{dt^l} = \sum_{l=1}^{m} p_l \frac{d^l\epsilon(t)}{dt^l}. \tag{35}$$

Eq. (35) is the nth-order differential equation for $\sigma(t)$, which, from a numerical standpoint, becomes more tractable than the convolutory forms implied by the use of the seismic attenuation models. Still, depending on the considered frequency range, the computational cost associated may be significant. To improve on the computational efficiency of the attenuation models, various approximations have been proposed [51–53].

More specifically, Day and Minster [51] used Padé approximations and obtained n ordinary differential equations for n additional internal variables. The sum of the internal variables multiplied by the unrelaxed modulus m_U provides a viscoelastic term additional to the elastic stress.

Emmerich and Korn [54] realized that an acceptable relaxation function corresponds to the rheology of what they defined as the generalized Maxwell body (GMB), which corresponds to n Maxwell bodies and a linear elastic spring (Hookean element) connected in parallel (Fig. 5). Given that any model comprising linear springs and dashpots connected in series or in parallel has its viscoelastic modulus in the form of a rational function of $i\omega$, the GMB allowed replacing the convolutory constitutive relation by a differential form.

Emmerich and Korn [54] obtained similar differential equations as Day and Minster [51]; to fit an arbitrary attenuation law $Q(\omega)$ they chose the relaxation frequencies logarithmically equidistant over a desired frequency range, and used the least-squares method to determine the weight factors of the relaxation mechanisms. Along the same lines, Carcione et al. [55,56] proposed the so-called generalized Zener bodies (GZB) comprising n Standard Linear Solids connected in parallel and in series. Mozco et al. [57] (2004) showed that both types of GZB yield identical attenuation laws with the GMB, and will not, therefore, be discussed any further.

4.4. Generalized Maxwell body

The complex modulus of the generalized Maxwell body, which comprises N Maxwell elements, each with stiffness E_l and viscosity η_l connected in parallel to a linear spring with stiffness E_H (see Fig. 5), is defined as

$$M(\omega) = E_H + \sum_{l=1}^{N} \frac{i\omega E_l}{\omega_l + i\omega}, \tag{36}$$

where $\omega_l = E_l/\eta_l$, and $l=1,\ldots,N$. The relaxed and unrelaxed moduli for this rheological model become

$$m_R = \lim_{\omega\to 0} M(\omega) = E_H, \quad m_U = \lim_{\omega\to\infty} M(\omega) = E_H + \sum_{l=1}^{N} E_l. \tag{37}$$

To incorporate the effects of nearly frequency-independent Q into time-domain numerical simulations of wave propagation, a set of particular relaxation functions are chosen [51,54] such that the complex viscoelastic modulus $M(\omega)$ is approximated as

$$M(\omega) = m_U\left(1-\sum_{l=1}^{N}\frac{w_l}{1+i\omega\tau_l}\right), \tag{38}$$

where τ_l denotes relaxation times, and w_l are weight coefficients. In this case, as shown in [51], the stress σ and strain ϵ have the following relationship:

$$\sigma(t) = m_U\left[\epsilon(t)-\sum_{l=1}^{N}\zeta_l\right], \tag{39}$$

where ζ_l is a memory variable. In turn, the memory variables follow first-order differential equations:

$$\tau_l\dot{\zeta}_l(t)+\zeta_l(t) = w_l\epsilon(t). \tag{40}$$

Liu and Archuleta [58] developed a procedure that uses an empirical interpolation relationship to calculate τ_l and w_l. More specifically, they used the definition of Q suggested by O'Connell and Budiansky [59] along with Eq. (38) to express Q in the frequency-domain as

$$Q(\omega) = \frac{\Re eM(\omega)}{\Im mM(\omega)} = \frac{1-\sum_{l=1}^{N}\frac{w_l}{1+(\omega\tau_l)^2}}{\sum_{l=1}^{N}\frac{\omega w_l\tau_l}{1+(\omega\tau_l)^2}}. \tag{41}$$

Next, they implemented the simulated annealing algorithm of Liu et al. [60] to find simultaneously N pairs of τ_l and w_l by minimizing the difference between the synthetic *nearly* frequency-independent $Q(\omega)$ given by Eq. (41) and a target Q model. Finally, they proposed an interpolation formula which, for a generalized Maxwell body with 8 Maxwell elements (GMB8), allows the estimation of the weight coefficients w_l through Eq. (42), where α_l, β_l, as well as τ_l in Eq. (41) are known quantities, and χ is given by Eq. (43) as a function of the target Q:

$$w_l = \chi(\chi\alpha_l+\beta_l), \tag{42}$$

$$\chi = \frac{3.071+1.433Q^{-1.158}\ln(Q/5)}{1+0.415Q}, \quad 5\le Q\le 5000. \tag{43}$$

The GMB8 succeeds in providing a very close approximation to a nearly frequency-independent Q. However, the level of temporal complexity implicated in the GMB8 makes its implementation in the context of full waveform inversion onerous. In this paper, we adopt a simpler two-element generalized Maxwell body (henceforth denoted as GMB2), which, as will be shown in Section 5, yields practically identical results to the GMB8 for wave propagation problems within the frequency range of interest for seismic applications, and overcomes the difficulties associated with the implementation of GMB8 for full waveform inversion problems in the near surface: as it can be readily seen from (35), the temporal complexity of the constitutive relation increases with the number of Maxwell elements in the GMB.

4.5. Two-element generalized Maxwell body (GMB2)

Consider the simpler generalized Maxwell body depicted in Fig. 6. The model consists of three elastic springs (E_1, E_2, E_3) and two dashpots (η_2,η_3) in such a way that one spring and two Maxwell models are connected in parallel. In this setting, the first

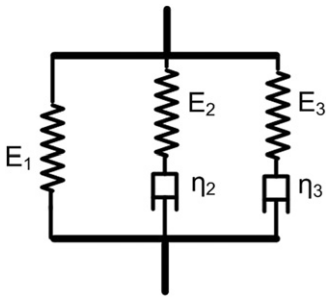

Fig. 6. A generalized Maxwell body with two Maxwell elements (GMB2).

spring (E_1) and the two Maxwell models ((E_2, η_2) and (E_3, η_3)) satisfy the following constitutive relations, respectively:

$$\sigma_1 = E_1\epsilon, \tag{44a}$$

$$\sigma_2+\frac{\eta_2}{E_2}\dot{\sigma_2} = \eta_2\dot{\epsilon}, \tag{44b}$$

$$\sigma_3+\frac{\eta_3}{E_3}\dot{\sigma_3} = \eta_3\dot{\epsilon}, \tag{44c}$$

where σ_1, σ_2, and σ_3 are the stresses in each of the elements, and ϵ is the total strain of the entire system. Applying the Fourier transform to Eqs. (44), and adding the individual terms, we obtain for the GMB2:

$$\hat{\sigma} = \hat{\sigma}_1+\hat{\sigma}_2+\hat{\sigma}_3 = \left(E_1+\frac{i\omega E_2\eta_2}{E_2+i\omega\eta_2}+\frac{i\omega E_3\eta_3}{E_3+i\omega\eta_3}\right)\hat{\epsilon}. \tag{45}$$

Next, the two relaxation time parameters τ_1 and τ_2 are defined as

$$\tau_1 = \frac{\eta_2}{E_2}, \quad \tau_2 = \frac{\eta_3}{E_3}. \tag{46}$$

Introducing (46) into (45), yields

$$\hat{\sigma}[1+(\tau_1+\tau_2)i\omega-\tau_1\tau_2\omega^2] = [E_1\{1+(\tau_1+\tau_2)i\omega-\tau_1\tau_2\omega^2\} + (\eta_2+\eta_3)i\omega-(E_2+E_3)\tau_1\tau_2\omega^2]\hat{\epsilon}. \tag{47}$$

On the other hand, the constitutive relation given by Eq. (39) for the generalized Maxwell model is simplified for GMB2 as follows:

$$\sigma(t) = m_U[\epsilon(t)-\zeta_1(t)-\zeta_2(t)], \tag{48}$$

where m_U is the unrelaxed modulus in accordance with the notation of the preceding sections, and $\zeta_1(t)$ and $\zeta_2(t)$ are the solutions of the following equations, respectively:

$$\tau_1\dot{\zeta}_1+\zeta_1 = w_1\epsilon, \tag{49a}$$

$$\tau_2\dot{\zeta}_2+\zeta_2 = w_2\epsilon. \tag{49b}$$

The unrelaxed modulus m_U can be obtained by taking the high-frequency limit of (47), i.e.:

$$m_U = E_1+E_2+E_3. \tag{50}$$

Applying the Fourier transform to both (48) and (49) results in

$$\hat{\sigma} = m_U(\hat{\epsilon}-\hat{\zeta}_1-\hat{\zeta}_2), \tag{51}$$

where

$$\hat{\zeta}_1 = \frac{w_1}{1+i\omega\tau_1}\hat{\epsilon}, \quad \hat{\zeta}_2 = \frac{w_2}{1+i\omega\tau_2}\hat{\epsilon}. \tag{52}$$

Combining (50)–(52) yields the following constitutive equation:

$$\hat{\sigma} = (E_1+E_2+E_3)\left(1-\frac{w_1}{1+i\omega\tau_1}-\frac{w_2}{1+i\omega\tau_2}\right)\hat{\epsilon}. \tag{53}$$

Table 1
Parameters α, β, τ_1 and τ_2 for various frequency bands to model *nearly* frequency-independent Q via GMB2.

Freq. band (Hz)	τ_1	τ_2	α	β
0.5–10	0.4500	0.0201	1.7680	−0.979
5–15	0.0400	0.0066	1.2640	−0.979
10–20	0.0200	0.0040	1.1972	−0.979
20–30	0.0108	0.0026	1.1291	−0.979

We determine the two constants w_1 and w_2 by equating (47) and (53). There results

$$w_1 = \frac{E_2}{E_1+E_2+E_3}, \quad w_2 = \frac{E_3}{E_1+E_2+E_3}. \tag{54}$$

Next, similarly to [58], we use a simplified expression for the weighting coefficients w_1 and w_2 as a function of the target Q factor as follows:

$$w_1 = w_2 = \alpha Q^{\beta}. \tag{55}$$

Subsequently, we select two frequencies ω_1 and ω_2 at which $Q(\omega)$ predicted by GMB2 is required to be equal to the value of the target Q, and seek to determine the parameters α, β, and the relaxation times τ_1 and τ_2. In this procedure, we assume that the shear wave velocity is measured at 1 Hz. Table 1 shows results of the fitting process for the frequency range of interest to earthquake engineering applications. We note that once the frequency range is selected, the parameters α, β, τ_1 and τ_2 can be selected from Table 1, and subsequently, the weight coefficients w_1 and w_2 can be computed using Eq. (55).

As a result of Eq. (55), we obtain

$$E_2 = E_3, \quad w_1 = w_2 = \frac{E_2}{E_1+2E_2} = \alpha Q^{\beta}. \tag{56}$$

Eq. (56) shows that the GMB2 depicted in Fig. 6 can be completely described by either of the pairs (E_1, E_2) or (E_1, Q) or (E_2, Q). If we take E_1 and E_2 as two independent material parameters, the damping coefficients η_2 and η_3 can be obtained from (46), as follows:

$$\eta_2 = \tau_1 E_2, \tag{57a}$$

$$\eta_3 = \tau_2 E_3, \tag{57b}$$

where τ_1 and τ_2 are constants within a certain frequency range of interest. By substituting (56) and (57) into (47), we obtain the constitutive equation in the frequency-domain for the GMB2 as

$$\hat{\sigma}[1+i\omega(\tau_1+\tau_2)-\omega^2\tau_1\tau_2] = [E_1+i\omega(\tau_1+\tau_2)(E_1+E_2)-\omega^2\tau_1\tau_2(E_1+2E_2)]\hat{\epsilon}. \tag{58}$$

We note that, by construction and prior to the fitting process, the GMB2 is characterized by five independent material constants (three spring and two dashpot constants). The process described above reduced the number of independent constants to only two. We remark that, in general, it is desirable that the number of independent spatially distributed material properties be kept to a minimum (while, of course, still maintaining consistency with the physics of the problem), so that there is a reasonable expectation that inverting for the properties will be successful (inverting for more than two independent properties will exact present-day algorithms and computational resources).

We also note that the described process could also be applied to the more accurate GMB8, and still yield a set of only two independent constants. This would have made the GMB8 an excellent candidate for modeling attenuation and for inversion, if it were not for the temporal complexity associated with the GMB8, as previously discussed.

5. Forward site response predictions with frequency-independent Q

In this section, we show examples of one-dimensional (1D) site response analyses, and compare the ground surface predictions obtained by means of the discussed simple rheological models to the response predicted by means of the frequency-domain solution with frequency independent Q. The 1D seismic wave propagation equations are evaluated using the central difference method, as described in [61]. Fig. 8 schematically illustrates the geometry and boundary conditions of the site response simulations conducted for a horizontally stratified system of homogeneous layers extending horizontally to infinity, and subjected to upward vertically propagating horizontally polarized shear (SH) waves.

The models investigated are the Maxwell, the Maxwell–Rayleigh model, the Standard Linear Solid model, the generalized Maxwell body with eight Maxwell elements [58] (GMB8), and the proposed generalized Maxwell body with two Maxwell elements (GMB2). For the rheological model parameters, we fit the Maxwell model attenuation at 1 Hz to the target Q, and the Maxwell–Rayleigh and Standard Linear Solid bodies at 0.5 Hz and 4 Hz. For the GMB8, we implement the interpolation algorithm proposed by Liu and Archuleta [58] to estimate the weight coefficients, and for the GMB2, we employ the approach proposed earlier in this paper. For all the models, the shear modulus (and shear wave velocity) is defined at 1 Hz. The attenuation laws predicted by each one of the rheological models for target $Q=25$ are compared in Fig. 7. As can be readily seen, the Maxwell, Maxwell–Rayleigh and Standard Linear Solid deviate substantially from the target Q both in the high and low frequency range. The proposed GMB2 approximates much better the target attenuation, whereas the GMB8 yields a practically frequency-independent Q across the entire frequency range.

The profiles used in the analyses are representative of deep sites in the Mississippi Embayment and have been adopted from Hashash and Park [62]; the velocity and attenuation variation with depth are shown in Fig. 9. More specifically, we investigate the response of three profiles with depths 100 m, 500 m, and 1 km overlying elastic bedrock with $V_s = 2700$ m/s, with fundamental frequencies at 1.1 Hz, 0.33 Hz, and 0.2 Hz, respectively. The damping ratios (quality factors) in the 0–30 m, 30–100 m and 100–1000 m ranges are 5%, 2% and 1%, respectively ($Q=10$, 25, and 50). In what follows, the three profiles are subjected to vertically incident SH seismic waves at the soil-bedrock interface, and their ground response is estimated using finite-difference viscoelastic simulations with each of the four rheological models described above; results are then compared to the frequency-domain

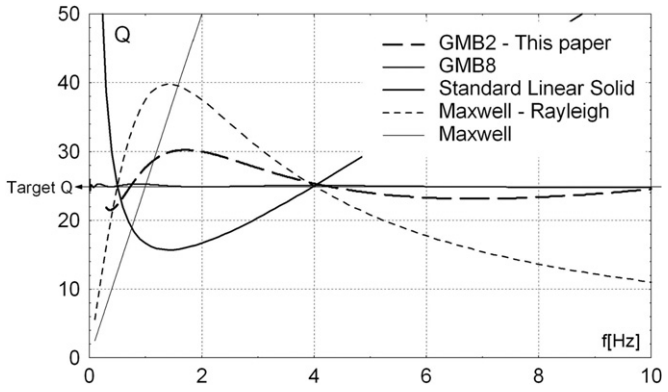

Fig. 7. Comparison of performance of various viscoelastic models investigated here in capturing nearly frequency-dependent Q. GMB8 corresponds to the generalized Maxwell body with interpolated weighting coefficients [58], and GMB2 is the two Maxwell element generalized body proposed in this paper.

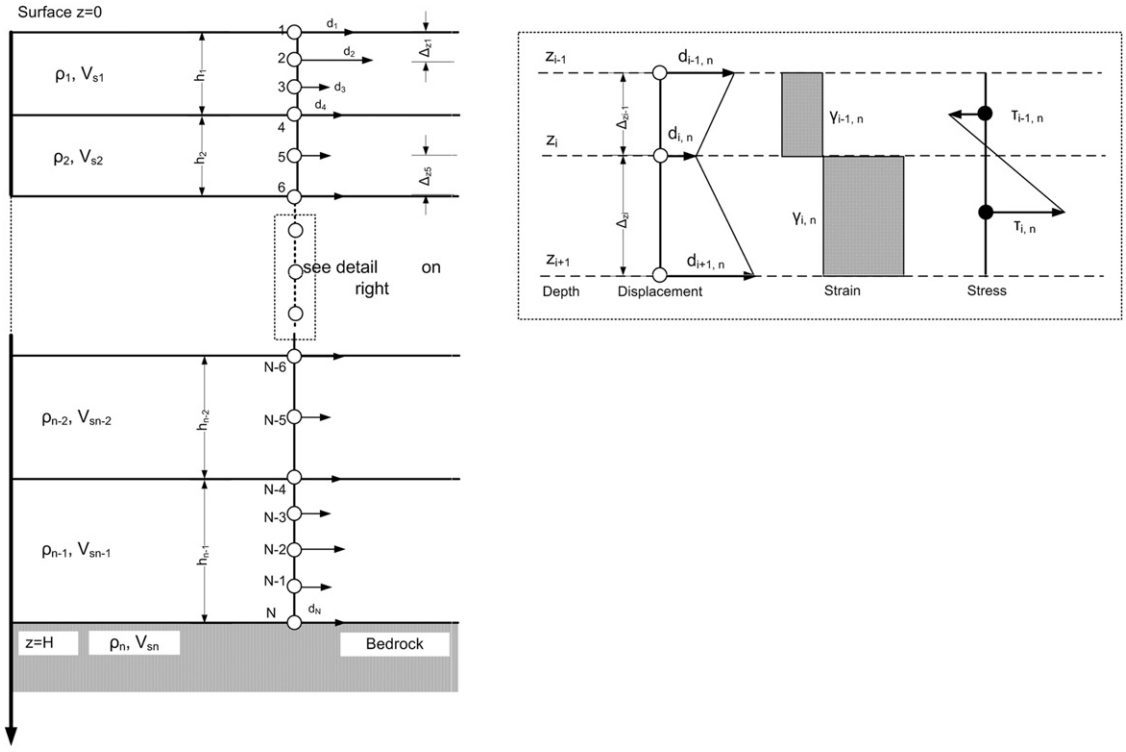

Fig. 8. Schematic representation of spatial discretization for a 1D soil deposit system, and detail illustrating the definition of displacement, strain and stress in the finite difference formulation. The displacement d and stress τ are evaluated at N grid nodes, which define sub-layers within layers. The displacement of node i at time step t_n is denoted $d(z_i,t_n)=d_{i,n}$, where z_i is the depth of node i. Similarly, the stress and strain at node i at time step t_n are denoted $\tau_{i,n}$ and $\gamma_{i,n}$ (modified from [61]).

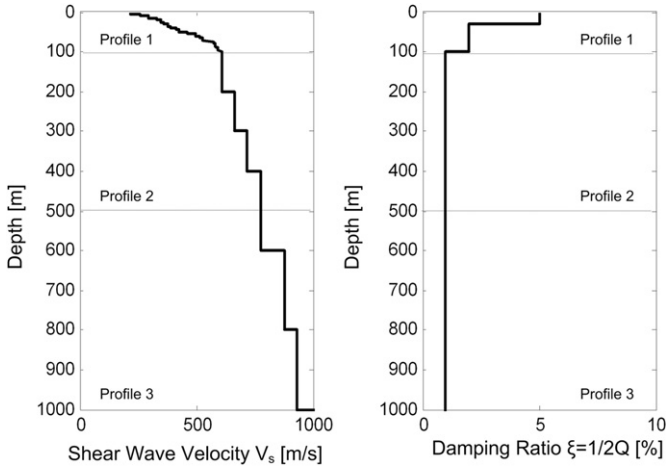

Fig. 9. Shear wave velocity and viscous damping profiles used in analyses. The variable profile properties are representative of conditions encountered in the Mississippi Embayment, Central US. The bedrock shear wave velocity is 2700 m/s (modified after Hashash and Park [62]).

solution of the wave equation with frequency-independent damping, considered to be the target response of the problem. The pure elastic solution (i.e. with zero damping) is also shown in the ensuing for comparison.

Seven synthetic motions with different frequency content are considered here in order to fully explore the performance of different models at different frequency bands. The seven input motions consist of a synthetic broadband seismic motion and six Ricker wavelets with predominant frequencies of 0.2, 0.5, 1.0, 2.0, 5.0, and 10.0 Hz. The time histories of these motions and corresponding Fourier amplitude spectra (FAS) are shown in Fig. 10. The shortest duration of the signal is 5 s to ensure that the incident motion can reach the surface to the soil column for the deepest profile.

Next, the results of the site response predictions are compared in terms of Fourier amplitude spectra of ground surface and surface-to-rock outcrop motion spectral ratios. For each of the 100 m, 500 m, and 1000 m profiles, representative results are illustrated in Figs. 11, 12, and 13, respectively. More specifically, Fig. 11a shows the ground response of the 100 m profile subjected to a Ricker wavelet with predominant frequency of 1 Hz. As shown in Fig. 10, this wavelet contains energy in the 0-2.5 Hz frequency range, and the resulting ground surface response predicted by the alternative Q models is similar. By contrast, Figs. 11b and c compare the ground response and site amplification of the 100 m profile subjected to a Ricker wavelet with predominant frequency of 10 Hz. In this case, the incident motion contains waveforms in the 0–20 Hz frequency range. The ground surface spectra highlight the large differences in the estimation of the attenuation law by the alternative rheological models depicted in Fig. 7.

More specifically, the purely elastic ($Q=\infty$) model gives the highest response in the 0–20 Hz frequency range, while the Maxwell model gives a response very close to the purely elastic in the frequency range greater than 2 Hz. The result is not surprising since the Maxwell model significantly overestimates Q (underestimates damping) in this frequency range. By contrast, the Maxwell–Rayleigh model gives the lowest response in the frequency range greater than 4 Hz, since it underpredicts Q in this frequency range. The Standard Linear Solid model gives a response lying between the Maxwell model response and exact frequency domain response, and this observation is also consistent with the Q fitting performance of these models: the Q value prediction of the SLS lies in between that of the Maxwell model and the target frequency-independent Q. The ground response prediction of the GMB8 model is the closest to the exact solution across the entire frequency range, with the exception of a small phase difference between the two solutions that increases as frequency increases and results from numerical dispersion. Finally, the GMB2 model, despite being much simpler than the

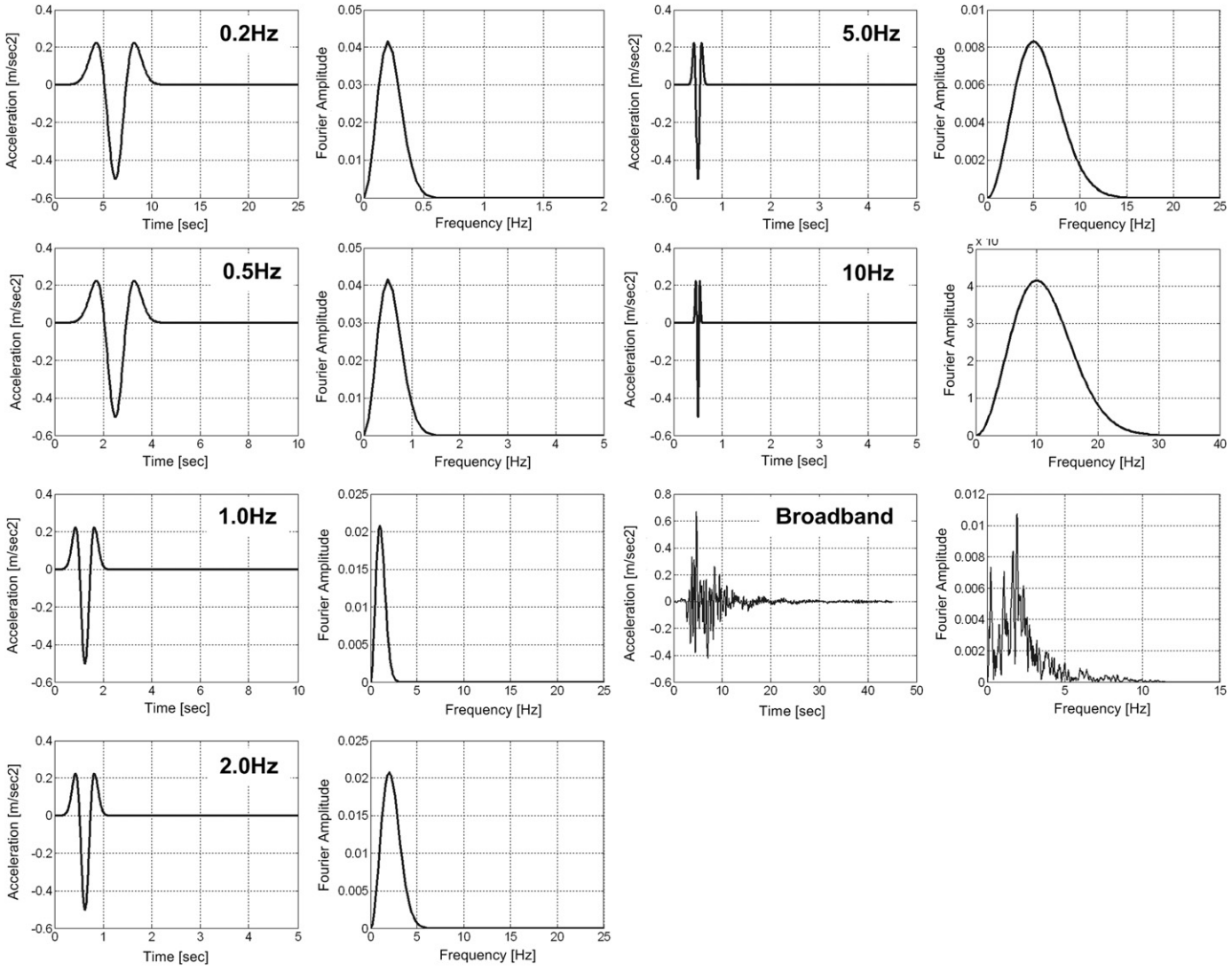

Fig. 10. Time histories and corresponding Fourier amplitude spectra of the incident motions used in the 1D site response simulations.

GMB8 model, gives a ground response prediction that is very close to that of GMB8 model. In the frequency range less than 3 Hz all the models predict very similar ground response; the wavelengths in this range are long enough to excite primarily the fundamental mode of the profile, and the resulting surface ground motion is not sensitive to the exact modeling of Q. Finally, Fig. 11d shows the site amplification ratio for the case of a broadband excitation. Results are very similar to Fig. 11c, since the broadband synthetic and the Ricker wavelet with predominant frequency 10 Hz contain energy in the same frequency range.

The observations made regarding Fig. 11 for the 100 m profile also apply to the 500 m and 1000 m profiles. The 500 m profile is subjected to a 0.5 Hz Ricker wavelet, a 5.0 Hz Ricker wavelet, and the same broadband ground motion as the 100 m profile, and the results are shown in Fig. 12. The 1000 m profile is subjected to a 0.2 Hz and a 2 Hz incident Ricker wavelet motions, and the same broadband synthetic seismogram, and the results are shown in Fig. 13.

Overall, as expected, the rheological model performance in fitting a frequency-independent target attenuation (Q) value improves with increasing complexity and number of model parameters. As a result, the selection of an optimal rheological model depends on the frequency content of incident motion, the amplification potential (transfer function) of the layered ground system, and the frequency band of interest. Consequently, the importance of modeling Q increases as the frequency range of ground motion becomes broader and as the profile becomes deeper, and simplified models such as the Maxwell, Maxwell–Rayleigh, and Standard Linear Solid may substantially overestimate or underestimate the predicted ground surface response. The proposed GMB2 rheological model provides a computationally efficient alternative to the more complex rheological systems (like the GMB8) or the seismic attenuation models of Section 4.1. The GMB2 yields practically identical ground surface response predictions irrespective of the frequency range of ground motion and characteristics of the soil profile at a substantially lower number of input parameters.

6. Simultaneous inversion for elastic and attenuation properties

In this section, we describe a systematic methodology for reconstructing the viscoelastic properties of the soil based on surficial measurements of the soil's response to probing excitation. Armed with the results of the forward site analyses that have lent credence to the GMB2 model, we use the constitutive equation (58) to represent the semi-infinite soil column's material

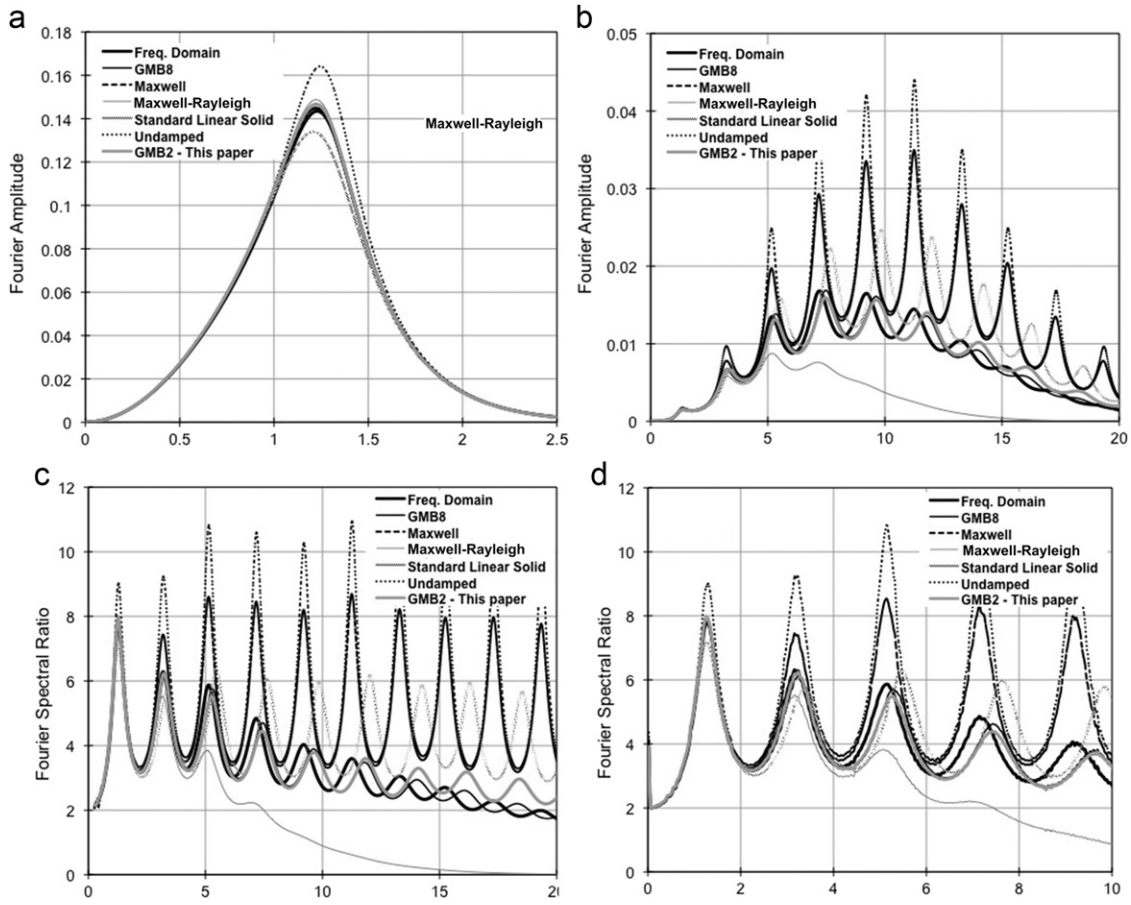

Fig. 11. Viscoelastic response of a 100 m deep profile: (a) ground surface response spectrum to an incident Ricker wavelet with central frequency 1 Hz; (b) ground surface response spectrum to an incident Ricker wavelet with central frequency 10 Hz; (c) site amplification for an incident Ricker wavelet with central frequency 10 Hz; (d) site amplification for an incident broadband synthetic ground motion.

behavior. To deal with the semi-infinite extent of the physical domains, we introduce truncation boundaries, and adopt perfectly matched-layers (PMLs) as the boundary wave absorbers. Fig. 14(a) depicts a one-dimensional semi-infinite soil medium, and Fig. 14(b) represents the corresponding PML-truncated domain, with truncation interface at $x=L$, and fixed boundary at $x=L_t$. For the forward wave simulation modeling in the PML-truncated domain, we develop PML-augmented wave equations based on complex coordinate stretching, similar to earlier work [63]. For the inverse wave modeling, we use a partial-differential-equation (PDE)-constrained optimization approach to reconstruct both the stiffness and attenuation characteristics of the soil. We discuss the details below.

6.1. Forward viscoelastic wave modeling using the GMB2 in PML-truncated domains

We first derive the PML-augmented equations governing the one-dimensional wave motion in viscoelastic solids that occupy the domain shown in Fig. 14(b). In [63], we discussed a mixed displacement–stress formulation that leads to a system of coupled PDEs in the time-domain. Their solution captures accurately the wave motion within the regular domain, while simultaneously enforcing rapid motion attenuation within the PML buffer zone. Here, we use the same procedure to arrive at the PML-augmented equations associated with the GMB2. Central to the formulation is the complex coordinate stretching, whereby the physical coordinate x is 'stretched' to become $\tilde{x}=x-i(c_{\mathrm{ref}}/\omega)\int_0^x g(s)\,ds$, where $g(x)$ is a wave attenuation function [63]; c_{ref} is a reference wave velocity of the soil medium. We start with the equilibrium equation and kinematic condition written in the frequency-domain:

$$\frac{d\hat{\sigma}}{dx}=-\omega^2\rho\hat{u}, \tag{59a}$$

$$\hat{\epsilon}=\frac{d\hat{u}}{dx}, \tag{59b}$$

and combine (58) and (59b) to yield

$$\hat{\sigma}[1+i\omega(\tau_1+\tau_2)-\omega^2\tau_1\tau_2] = [E_1+i\omega(\tau_1+\tau_2)(E_1+E_2)-\omega^2\tau_1\tau_2(E_1+2E_2)]\frac{d\hat{u}}{dx}. \tag{60}$$

Next, we apply complex coordinate stretching to (59a) and (60), respectively (see [63] for details): we rewrite both equations using the complex-stretched coordinate $\tilde{x}$, i.e., we replace x with $\tilde{x}$ in each of the equations using the stretching function $\lambda(x)$ per:

$$\frac{d}{d\tilde{x}}=\frac{1}{\lambda(x)}\frac{d}{dx} \quad \text{with } \lambda(x)=1-i\frac{c_{\mathrm{ref}}g(x)}{\omega}=1-i\frac{h(x)}{\omega}. \tag{61}$$

There results

$$\frac{1}{\lambda(x)}\frac{d\hat{\sigma}}{dx}=-\omega^2\rho\hat{u}, \tag{62}$$

$$\hat{\sigma}[1+i\omega(\tau_1+\tau_2)-\omega^2\tau_1\tau_2] = [E_1+i\omega(\tau_1+\tau_2)(E_1+E_2)-\omega^2\tau_1\tau_2(E_1+2E_2)]\frac{1}{\lambda(x)}\frac{d\hat{u}}{dx}. \tag{63}$$

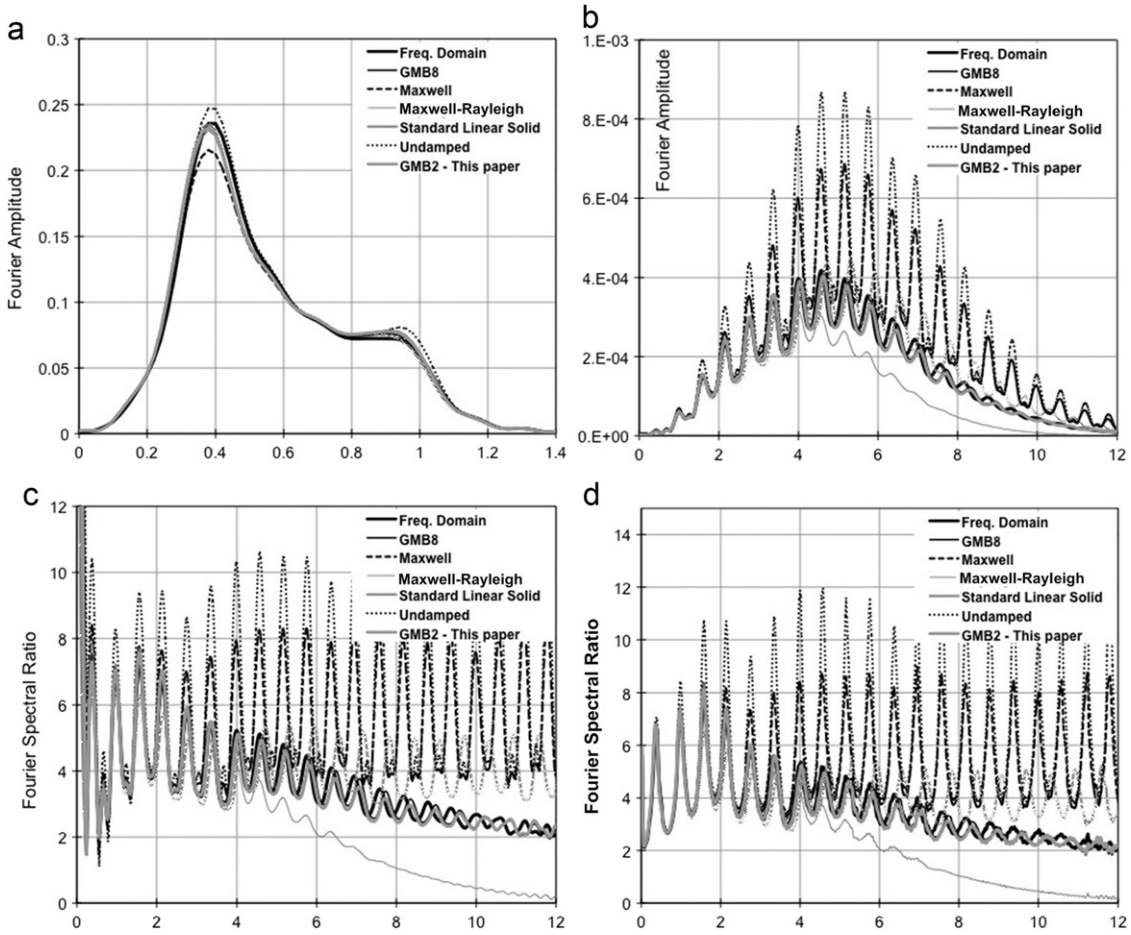

Fig. 12. Viscoelastic response of a 500 m deep profile: (a) ground surface response spectrum to an incident Ricker wavelet with central frequency 0.5 Hz; (b) ground surface response spectrum to an incident Ricker wavelet with central frequency 5 Hz; (c) site amplification for an incident Ricker wavelet with central frequency 5 Hz; (d) site amplification for an incident broadband synthetic ground motion.

Multiplying by $\lambda(x)$ both sides of (62) and of (63), while considering (61), results in

$$\frac{d\hat{\sigma}}{dx} = -\omega^2\rho\hat{u} + i\omega\rho h\hat{u}, \tag{64}$$

$$\frac{1}{i\omega}h\hat{\sigma} + [1+h(\tau_1+\tau_2)]\hat{\sigma} + i\omega(\tau_1+\tau_2+h\tau_1\tau_2)\hat{\sigma} - \omega^2\tau_1\tau_2\hat{\sigma} = E_1\frac{d\hat{u}}{dx} + i\omega(\tau_1+\tau_2)(E_1+E_2)\frac{d\hat{u}}{dx} - \omega^2\tau_1\tau_2(E_1+2E_2)\frac{d\hat{u}}{dx}. \tag{65}$$

Eqs. (64) and (65) are next inverted back to the time-domain to yield

$$\rho\frac{\partial^2 u}{\partial t^2} + \rho h\frac{\partial u}{\partial t} - \frac{\partial\sigma}{\partial x} = 0, \tag{66}$$

$$h\int_0^t \sigma(x,z)\,dz + [1+h(\tau_1+\tau_2)]\sigma + (\tau_1+\tau_2+h\tau_1\tau_2)\frac{\partial\sigma}{\partial t} + \tau_1\tau_2\frac{\partial^2\sigma}{\partial t^2} = E_1\frac{\partial u}{\partial x} + (\tau_1+\tau_2)(E_1+E_2)\frac{\partial^2 u}{\partial x\partial t} + \tau_1\tau_2(E_1+2E_2)\frac{\partial^3 u}{\partial x\partial t^2}. \tag{67}$$

Eq. (67) includes a term that requires the temporal integration of stress, i.e., $\int_0^t \sigma(x,z)\,dz$. For the treatment of this term, we define an auxiliary stress-memory term $\overline{\sigma}$ as

$$\overline{\sigma} = \int_0^t \sigma(x,z)\,dz. \tag{68}$$

By substituting (68) into (67), we obtain

$$\tau_1\tau_2\frac{\partial^2\sigma}{\partial t^2} + (\tau_1+\tau_2+h\tau_1\tau_2)\frac{\partial\sigma}{\partial t} + [1+h(\tau_1+\tau_2)]\sigma + h\overline{\sigma} - E_1\frac{\partial u}{\partial x} - (\tau_1+\tau_2)(E_1+E_2)\frac{\partial^2 u}{\partial x\partial t} - \tau_1\tau_2(E_1+2E_2)\frac{\partial^3 u}{\partial x\partial t^2} = 0. \tag{69}$$

Eqs. (66) and (69) are displacement–stress mixed equations governing the propagation of waves in *one-dimensional viscoelastic PML-truncated domains*. Referring to Fig. 14(b), the forward problem associated with the GMB2 in a one-dimensional PML-truncated semi-infinite domain can then be stated as follows:

Find $u \equiv u(x,t)$ and $\sigma \equiv \sigma(x,t)$, such that

$$\rho\frac{\partial^2 u}{\partial t^2} + \rho h\frac{\partial u}{\partial t} - \frac{\partial\sigma}{\partial x} = 0 \quad \text{for } x\in(0,L_t),\ t\in(0,T], \tag{70}$$

$$\tau_1\tau_2\frac{\partial^2\sigma}{\partial t^2} + (\tau_1+\tau_2+h\tau_1\tau_2)\frac{\partial\sigma}{\partial t} + [1+h(\tau_1+\tau_2)]\sigma + h\overline{\sigma} - E_1\frac{\partial u}{\partial x} - (\tau_1+\tau_2)(E_1+E_2)\frac{\partial^2 u}{\partial x\partial t} - \tau_1\tau_2(E_1+2E_2)\frac{\partial^3 u}{\partial x\partial t^2} = 0, \quad \text{for } x\in(0,L_t),\ t\in(0,T], \tag{71}$$

with

$$u(L_t,t) = 0, \tag{72a}$$

$$\sigma(0,t) = p(t), \tag{72b}$$

$$u(x,0) = \frac{\partial u}{\partial t}(x,0) = 0, \tag{72c}$$

$$\overline{\sigma}(x,0) = \sigma(x,0) = \frac{\partial\sigma}{\partial t}(x,0) = 0. \tag{72d}$$

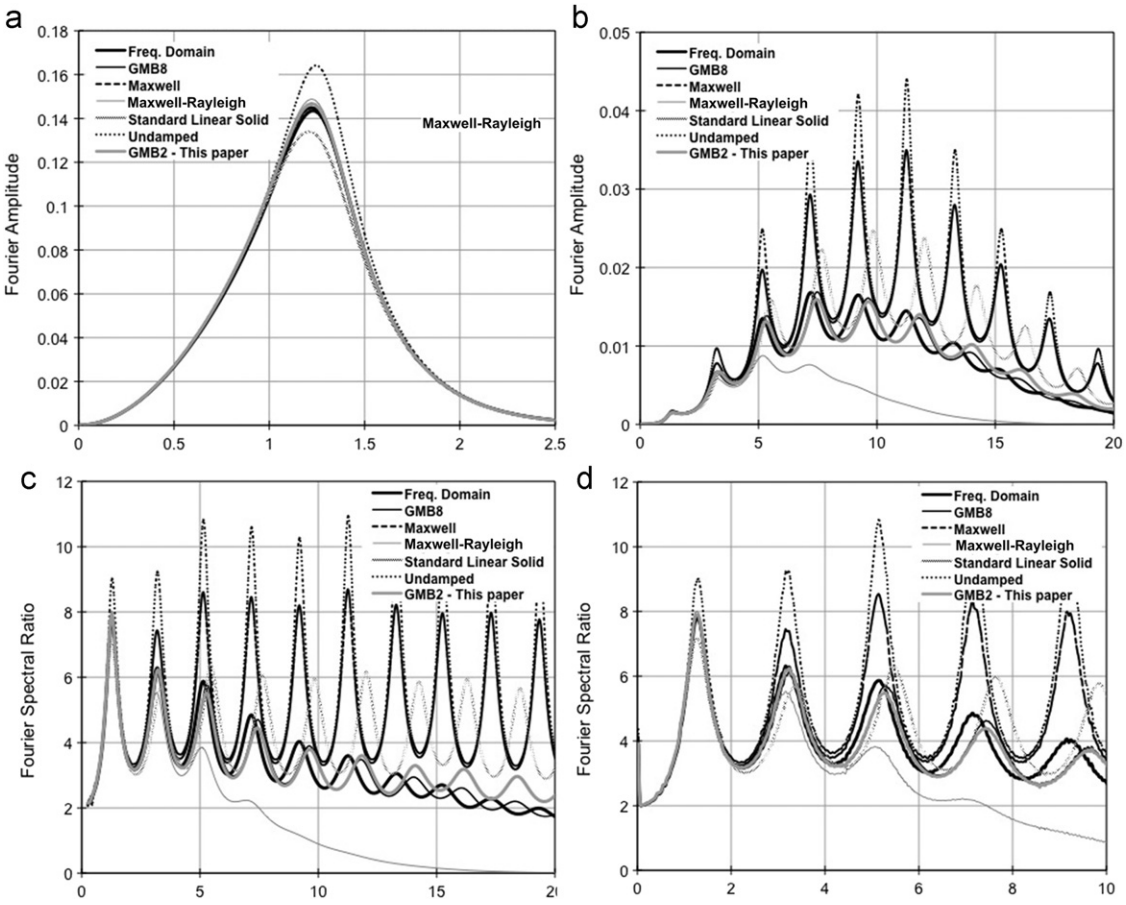

Fig. 13. Viscoelastic response of a 1000 m deep profile: (a) ground surface response spectrum to an incident Ricker wavelet with central frequency 0.2 Hz; (b) ground surface response spectrum to an incident Ricker wavelet with central frequency 2 Hz; (c) site amplification for an incident Ricker wavelet with central frequency 2 Hz; (d) site amplification for an incident broadband synthetic ground motion.

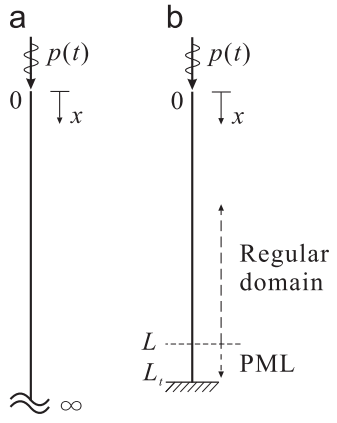

Fig. 14. (a) A one-dimensional semi-infinite soil domain, and (b) the corresponding PML-truncated domain subject to a tip stress load $p(t)$.

6.2. The inverse problem for the viscoelastic medium

6.2.1. The least-squares misfit

Referring to Fig. 14(b), the inverse problem for reconstructing the viscoelastic parameters E_1 and E_2 of the GMB2 in the PML-truncated domain can be cast as follows:

Minimize:

$$\mathcal{J} := \frac{1}{2}\int_0^T [u(0,t)-u_m(0,t)]^2\, dt + \mathcal{R}_{E_1}(E_1)+\mathcal{R}_{E_2}(E_2), \tag{73}$$

subject to (70)–(72).

In (73), $u_m(0,t)$ is the measured surface response to a known excitation $p(t)$, and $u(0,t)$ is the computed response corresponding to assumed trial profiles $E_1(x)$ and $E_2(x)$. In addition to the response misfit, $\mathcal{J}$ comprises two regularization terms with respect to E_1 and E_2, respectively. When total variation (TV) regularization is used, $\mathcal{R}_{E_1}$ and $\mathcal{R}_{E_2}$ are

$$\mathcal{R}_{E_1} = R_{E_1}\int_0^{L_t}\left[\left(\frac{dE_1}{dx}\right)^2+\epsilon\right]^{1/2} dx, \tag{74}$$

$$\mathcal{R}_{E_2} = R_{E_2}\int_0^{L_t}\left[\left(\frac{dE_2}{dx}\right)^2+\epsilon\right]^{1/2} dx, \tag{75}$$

where R_{E_1} and R_{E_2} are regularization factors for E_1 and E_2, respectively. When Tikhonov (TN) regularization is used, the corresponding terms become

$$\mathcal{R}_{E_1} = R_{E_1}\int_0^{L_t}\left(\frac{dE_1}{dx}\right)^2 dx, \tag{76}$$

$$\mathcal{R}_{E_2} = R_{E_2}\int_0^{L_t}\left(\frac{dE_2}{dx}\right)^2 dx. \tag{77}$$

Next, we seek to minimize $\mathcal{J}$ in an attempt to reconstruct the soil's viscoelastic material properties $E_1(x)$ and $E_2(x)$.

6.2.2. The Lagrangian functional

To tackle the PDE-constrained optimization problem defined in (73), we construct a Lagrangian functional $\mathcal{L}$, where the misfit

functional $\mathcal{J}$ is augmented by the weak imposition of the governing PDEs and boundary conditions, per:

$$\mathcal{L}(u,\sigma,\lambda_u,\lambda_\sigma,\lambda_B,E_1,E_2)=\frac{1}{2}\int_0^T [u(0,t)-u_m(0,t)]^2\,dt+\mathcal{R}_{E_1}(E_1)+\mathcal{R}_{E_2}(E_2)$$
$$+\int_0^{L_t}\int_0^T \lambda_u\left[\rho\frac{\partial^2 u}{\partial t^2}+\rho h\frac{\partial u}{\partial t}-\frac{\partial \sigma}{\partial x}\right]dt\,dx$$
$$+\int_0^{L_t}\int_0^T \lambda_\sigma\left[\tau_1\tau_2\frac{\partial^2\sigma}{\partial t^2}+(\tau_1+\tau_2+h\tau_1\tau_2)\frac{\partial\sigma}{\partial t}+[1+h(\tau_1+\tau_2)]\sigma+h\overline{\sigma}\right.$$
$$\left.-E_1\frac{\partial u}{\partial x}-(\tau_1+\tau_2)(E_1+E_2)\frac{\partial^2 u}{\partial x\partial t}-\tau_1\tau_2(E_1+2E_2)\frac{\partial^3 u}{\partial x\partial t^2}\right]dt\,dx$$
$$+\int_0^T \lambda_B[\sigma(0,t)-p(t)]\,dt, \tag{78}$$

where λ_u, λ_σ, and λ_B are Lagrange multipliers used to side-impose the governing PDEs (70), (71) and the boundary condition (72b). The remaining boundary and initial conditions (72a), (72c), and (72d) will be explicitly imposed in the semi-discrete forms. We then seek to satisfy the stationarity of $\mathcal{L}$, by requiring that the first variations of $\mathcal{L}$ vanish. There result the following first-order optimality conditions:

6.2.3. The first optimality condition

We enforce the vanishing of the variation of $\mathcal{L}$ with respect to the Lagrange multipliers λ_u, λ_σ, and λ_B, i.e.,

$$\delta_{\lambda_u}\mathcal{L}=0,\quad \delta_{\lambda_\sigma}\mathcal{L}=0,\quad \delta_{\lambda_B}\mathcal{L}=0. \tag{79}$$

Eqs. (79) result in the *mixed state (or forward) problem*, identical to the initial- and boundary-value problem (IBVP) defined by (70), (71), and (72).

6.2.4. The second optimality condition

Similarly, we require the vanishing of the variation of $\mathcal{L}$ with respect to the state variables u and σ, i.e.,

$$\delta_u\mathcal{L}=0,\quad \delta_\sigma\mathcal{L}=0, \tag{80}$$

which result in the following *mixed adjoint problem*:

Find $\lambda_u\equiv\lambda_u(x,t)$ and $\lambda_\sigma\equiv\lambda_\sigma(x,t)$, such that

$$\rho\frac{\partial^2\lambda_u}{\partial t^2}-\rho h\frac{\partial\lambda_u}{\partial t}+\frac{\partial\Theta}{\partial x}=0\quad \text{for } x\in(0,L_t),\ t\in[0,T), \tag{81}$$

$$\tau_1\tau_2\frac{\partial^2\lambda_\sigma}{\partial t^2}-(\tau_1+\tau_2+h\tau_1\tau_2)\frac{\partial\lambda_\sigma}{\partial t}+[1+h(\tau_1+\tau_2)]\lambda_\sigma$$
$$-h\overline{\lambda}_\sigma+\frac{\partial\lambda_u}{\partial x}=0\quad \text{for } x\in(0,L_t),\ t\in[0,T), \tag{82}$$

with

$$\lambda_u(L_t,t)=0, \tag{83a}$$

$$\Theta(0,t)=u(0,t)-u_m(0,t), \tag{83b}$$

$$\lambda_u(x,T)=\frac{\partial\lambda_u}{\partial t}(x,T)=0, \tag{83c}$$

$$\overline{\lambda}_\sigma(x,T)=\lambda_\sigma(x,T)=\frac{\partial\lambda_\sigma}{\partial t}(x,T)=0, \tag{83d}$$

where

$$\Theta(x,t)=E_1\lambda_\sigma-(\tau_1+\tau_2)(E_1+E_2)\frac{\partial\lambda_\sigma}{\partial t}$$
$$+\tau_1\tau_2(E_1+2E_2)\frac{\partial^2\lambda_\sigma}{\partial t^2}, \tag{84}$$

$$\overline{\lambda}_\sigma=\int_0^T \lambda_\sigma(x,z)\,dz. \tag{85}$$

We note that the adjoint problem is driven by the misfit between the computed and observed responses (83b). Moreover, it is a final-value problem, as opposed to the initial-value state problem. The adjoint equations are also mixed (λ_u and λ_σ) and PML-endowed.

6.2.5. The third optimality condition

Lastly, we impose the vanishing of the variation of $\mathcal{L}$ with respect to the material parameters E_1 and E_2, i.e.,

$$\delta_{E_1}\mathcal{L}=0,\quad \delta_{E_2}\mathcal{L}=0, \tag{86}$$

which entails the following time-independent *control problems*[2]:

$$-R_{E_1}\epsilon\frac{d^2E_1}{dx^2}\left[\left(\frac{dE_1}{dx}\right)^2+\epsilon\right]^{-3/2}$$
$$+\int_0^T\left[-\lambda_\sigma\frac{\partial u}{\partial x}+(\tau_1+\tau_2)\frac{\partial\lambda_\sigma}{\partial t}\frac{\partial u}{\partial x}+\tau_1\tau_2\frac{\partial\lambda_\sigma}{\partial t}\frac{\partial^2 u}{\partial x\partial t}\right]dt=0, \tag{87a}$$

$$\frac{dE_1}{dx}(0)=\frac{dE_1}{dx}(L_t)=0, \tag{87b}$$

and

$$-R_{E_2}\epsilon\frac{d^2E_2}{dx^2}\left[\left(\frac{dE_2}{dx}\right)^2+\epsilon\right]^{-3/2}$$
$$+\int_0^T\left[(\tau_1+\tau_2)\frac{\partial\lambda_\sigma}{\partial t}\frac{\partial u}{\partial x}+2\tau_1\tau_2\frac{\partial\lambda_\sigma}{\partial t}\frac{\partial^2 u}{\partial x\partial t}\right]dt=0, \tag{88a}$$

$$\frac{dE_2}{dx}(0)=\frac{dE_2}{dx}(L_t)=0. \tag{88b}$$

We remark that the left-hand-side of (87a) becomes the continuous form of the reduced gradient in the space of the control variable E_1, i.e.,

$$\nabla_{E_1}\mathcal{L}=-R_{E_1}\epsilon\frac{d^2E_1}{dx^2}\left[\left(\frac{dE_1}{dx}\right)^2+\epsilon\right]^{-3/2}$$
$$+\int_0^T\left[-\lambda_\sigma\frac{\partial u}{\partial x}+(\tau_1+\tau_2)\frac{\partial\lambda_\sigma}{\partial t}\frac{\partial u}{\partial x}+\tau_1\tau_2\frac{\partial\lambda_\sigma}{\partial t}\frac{\partial^2 u}{\partial x\partial t}\right]dt. \tag{89}$$

Similarly, the left-hand-side of (88a) becomes the continuous form of the reduced gradient in the space of E_2, i.e.,

$$\nabla_{E_2}\mathcal{L}=-R_{E_2}\epsilon\frac{d^2E_2}{dx^2}\left[\left(\frac{dE_2}{dx}\right)^2+\epsilon\right]^{-3/2}$$
$$+\int_0^T\left[(\tau_1+\tau_2)\frac{\partial\lambda_\sigma}{\partial t}\frac{\partial u}{\partial x}+2\tau_1\tau_2\frac{\partial\lambda_\sigma}{\partial t}\frac{\partial^2 u}{\partial x\partial t}\right]dt. \tag{90}$$

Once the state and adjoint solutions are obtained, the reduced gradients (89) and (90) can be used to update the material distributions $E_1(x)$ and $E_2(x)$, respectively.

6.2.6. Semi-discrete form of the state problem

We use a mixed finite element method to obtain the approximate solutions for u and σ in the state problem described by the IBVP (70)–(72). We seek $u\simeq u_h\in H^h\subset H^1(\Omega)$ and $\sigma\simeq\sigma_h\in Q^h\subset L^2(\Omega)$ such that (70) and (71) be satisfied. We multiply (70) and (71) by appropriate test functions $w(x)$ and $q(x)$, and then integrate over the entire domain $(0,L_t)$ in order to arrive at the corresponding weak forms:

$$\int_0^{L_t} w\left[\rho\frac{\partial^2 u}{\partial t^2}+\rho h\frac{\partial u}{\partial t}\right]dx+\int_0^{L_t}\frac{dw}{dx}\sigma\,dx=-w(0)p(t), \tag{91}$$

[2] We write the control problems only for the case of the TV regularization; the TN case is simpler [63].

$$\int_0^{L_t} \tau_1\tau_2 q\frac{\partial^2\sigma}{\partial t^2}\,dx+\int_0^{L_t}(\tau_1+\tau_2+h\tau_1\tau_2)q\frac{\partial\sigma}{\partial t}\,dx + \int_0^{L_t}\left[1+h(\tau_1+\tau_2)\right]q\sigma\,dx+\int_0^{L_t} hq\overline{\sigma}\,dx-\int_0^{L_t} E_1 q\frac{\partial u}{\partial x}\,dx - \int_0^{L_t}(\tau_1+\tau_2)(E_1+E_2)q\frac{\partial^2 u}{\partial x\partial t}\,dx - \int_0^{L_t}\tau_1\tau_2(E_1+2E_2)q\frac{\partial^3 u}{\partial x\partial t^2}\,dx=0. \tag{92}$$

In (91) and (92), u and σ are approximated as

$$u(x,t)\simeq\boldsymbol{\phi}^{\mathrm{T}}(x)\mathbf{u}(t),\quad \sigma(x,t)\simeq\boldsymbol{\psi}^{\mathrm{T}}(x)\boldsymbol{\sigma}(t), \tag{93}$$

where $\boldsymbol{\phi}$ and $\boldsymbol{\psi}$ are vectors of approximants associated with nodal displacements $\mathbf{u}$ and nodal stresses $\boldsymbol{\sigma}$, respectively. The two test functions $w(x)$ and $q(x)$ are similarly discretized by the same approximants $\boldsymbol{\phi}$ and $\boldsymbol{\psi}$, i.e.,

$$w(x)\simeq\mathbf{w}^{\mathrm{T}}\boldsymbol{\phi}(x),\quad q(x)\simeq\mathbf{q}^{\mathrm{T}}\boldsymbol{\psi}(x). \tag{94}$$

We chose a pair of quadratic approximants for both $\boldsymbol{\phi}$ and $\boldsymbol{\psi}$, which numerically have shown to be stable. Introducing the approximants in (91) and (92) results in the following semi-discrete form:

$$\mathbf{M}^{\mathrm{st}}\ddot{\mathbf{d}}^{\mathrm{st}}+\mathbf{C}^{\mathrm{st}}\dot{\mathbf{d}}^{\mathrm{st}}+\mathbf{K}^{\mathrm{st}}\mathbf{d}^{\mathrm{st}}+\mathbf{G}^{\mathrm{st}}\overline{\mathbf{d}}^{\mathrm{st}}=\mathbf{R}^{\mathrm{st}}, \tag{95}$$

where

$$\mathbf{M}^{\mathrm{st}}=\begin{bmatrix}\int_0^{L_t}\rho\boldsymbol{\phi}\boldsymbol{\phi}^{\mathrm{T}}\,dx & \mathbf{0}\\ -\int_0^{L_t}\kappa_1\boldsymbol{\psi}\frac{\partial\boldsymbol{\phi}^{\mathrm{T}}}{\partial x}\,dx & \int_0^{L_t}\tau_1\tau_2\boldsymbol{\psi}\boldsymbol{\psi}^{\mathrm{T}}\,dx\end{bmatrix}, \tag{96}$$

$$\mathbf{C}^{\mathrm{st}}=\begin{bmatrix}\int_0^{L_t}\rho h\boldsymbol{\phi}\boldsymbol{\phi}^{\mathrm{T}}\,dx & \mathbf{0}\\ -\int_0^{L_t}\kappa_2\boldsymbol{\psi}\frac{\partial\boldsymbol{\phi}^{\mathrm{T}}}{\partial x}\,dx & \int_0^{L_t}\kappa_3\boldsymbol{\psi}\boldsymbol{\psi}^{\mathrm{T}}\,dx\end{bmatrix}, \tag{97}$$

$$\mathbf{K}^{\mathrm{st}}=\begin{bmatrix}\mathbf{0} & \int_0^{L_t}\frac{\partial\boldsymbol{\phi}}{\partial x}\boldsymbol{\psi}^{\mathrm{T}}\,dx\\ -\int_0^{L_t}E_1\boldsymbol{\psi}\frac{\partial\boldsymbol{\phi}^{\mathrm{T}}}{\partial x}\,dx & \int_0^{L_t}\kappa_4\boldsymbol{\psi}\boldsymbol{\psi}^{\mathrm{T}}\,dx\end{bmatrix}, \tag{98}$$

$$\mathbf{G}^{\mathrm{st}}=\begin{bmatrix}\mathbf{0} & \mathbf{0}\\ \mathbf{0} & \int_0^{L_t}h\boldsymbol{\psi}\boldsymbol{\psi}^{\mathrm{T}}\,dx\end{bmatrix}, \tag{99}$$

$$\mathbf{R}^{\mathrm{st}}=\begin{bmatrix}-\boldsymbol{\phi}(0)p(t)\\ \mathbf{0}\end{bmatrix}, \tag{100}$$

$$\mathbf{d}^{\mathrm{st}}=\begin{bmatrix}\mathbf{u}\\ \boldsymbol{\sigma}\end{bmatrix},\quad \overline{\mathbf{d}}^{\mathrm{st}}=\begin{bmatrix}\overline{\mathbf{u}}\\ \overline{\boldsymbol{\sigma}}\end{bmatrix}, \tag{101}$$

$$\kappa_1=\tau_1\tau_2(E_1+2E_2), \tag{102a}$$

$$\kappa_2=(\tau_1+\tau_2)(E_1+E_2), \tag{102b}$$

$$\kappa_3=\tau_1+\tau_2+h\tau_1\tau_2, \tag{102c}$$

$$\kappa_4=1+h(\tau_1+\tau_2). \tag{102d}$$

In (95), $\mathbf{M}^{\mathrm{st}}$, $\mathbf{C}^{\mathrm{st}}$, and $\mathbf{K}^{\mathrm{st}}$ represent the mass-like, damping-like, and stiffness-like matrices of the semi-discrete form of the state problem, respectively. $\mathbf{d}^{\mathrm{st}}$ is a vector of nodal unknowns comprising nodal displacements $\mathbf{u}$ and stresses $\boldsymbol{\sigma}$. $\mathbf{G}^{\mathrm{st}}$ is an additional system matrix associated with a vector $\overline{\mathbf{d}}^{\mathrm{st}}$ comprising nodal displacement- and stress-memories ($\overline{\mathbf{u}}$ and $\overline{\boldsymbol{\sigma}}$). $\overline{\mathbf{u}}$ is a vector of nodal displacement-memories representing the temporal integration of displacements ($\overline{u}=\int_0^t u(x,z)\,dz$), defined similarly as to the stress memory $\overline{\sigma}$ (68). $\mathbf{R}^{\mathrm{st}}$ denotes a load vector. The superscript 'st' stands for the *state problem*. We use a third-order time integration scheme [64] to implement the semi-discrete form (95) of the initial-value state problem (see Appendix for the details).

6.2.7. Semi-discrete form of the adjoint problem

We use the same mixed method for the approximate solutions of λ_u and λ_σ in the adjoint problem. We seek $\lambda_u\simeq(\lambda_u)_h\in H^h\subset H^1(\Omega)$ and $\lambda_\sigma\simeq(\lambda_\sigma)_h\in Q^h\subset L^2(\Omega)$ such that (81) and (82) be satisfied. Using the same test functions $w(x)$ and $q(x)$, the weak forms are derived as

$$\int_0^{L_t} w\left[\rho\frac{\partial^2\lambda_u}{\partial t^2}-\rho h\frac{\partial\lambda_u}{\partial t}\right]dx-\int_0^{L_t}\frac{dw}{dx}\Theta\,dx = -w(0)[u(0,t)-u_m(0,t)], \tag{103}$$

$$\int_0^{L_t}\tau_1\tau_2 q\frac{\partial^2\lambda_\sigma}{\partial t^2}\,dx-\int_0^{L_t}(\tau_1+\tau_2+h\tau_1\tau_2)q\frac{\partial\lambda_\sigma}{\partial t}\,dx + \int_0^{L_t}\left[1+h(\tau_1+\tau_2)\right]q\lambda_\sigma\,dx-\int_0^{L_t}hq\overline{\lambda_\sigma}\,dx+\int_0^{L_t}q\frac{\partial\lambda_u}{\partial x}\,dx=0. \tag{104}$$

In (103) and (104), λ_u and λ_σ are approximated as

$$\lambda_u(x,t)\simeq\boldsymbol{\phi}^{\mathrm{T}}(x)\boldsymbol{\lambda}_u(t),\quad \lambda_\sigma(x,t)\simeq\boldsymbol{\psi}^{\mathrm{T}}(x)\boldsymbol{\lambda}_\sigma(t), \tag{105}$$

where $\boldsymbol{\phi}$ and $\boldsymbol{\psi}$ are vectors of approximants associated with nodal values of λ_u and λ_σ, respectively. The test functions and the interpolation order are the same as in the case of the mixed state problem. There results the following semi-discrete form:

$$\mathbf{M}^{\mathrm{ad}}\ddot{\mathbf{d}}^{\mathrm{ad}}+\mathbf{C}^{\mathrm{ad}}\dot{\mathbf{d}}^{\mathrm{ad}}+\mathbf{K}^{\mathrm{ad}}\mathbf{d}^{\mathrm{ad}}+\mathbf{G}^{\mathrm{ad}}\overline{\mathbf{d}}^{\mathrm{ad}}=\mathbf{R}^{\mathrm{ad}}, \tag{106}$$

where

$$\mathbf{M}^{\mathrm{ad}}=\begin{bmatrix}\int_0^{L_t}\rho\boldsymbol{\phi}\boldsymbol{\phi}^{\mathrm{T}}\,dx & -\int_0^{L_t}\kappa_1\frac{\partial\boldsymbol{\phi}}{\partial x}\boldsymbol{\psi}^{\mathrm{T}}\,dx\\ \mathbf{0} & \int_0^{L_t}\tau_1\tau_2\boldsymbol{\psi}\boldsymbol{\psi}^{\mathrm{T}}\,dx\end{bmatrix}, \tag{107}$$

$$\mathbf{C}^{\mathrm{ad}}=\begin{bmatrix}-\int_0^{L_t}\rho h\boldsymbol{\phi}\boldsymbol{\phi}^{\mathrm{T}}\,dx & \int_0^{L_t}\kappa_2\frac{\partial\boldsymbol{\phi}}{\partial x}\boldsymbol{\psi}^{\mathrm{T}}\,dx\\ \mathbf{0} & -\int_0^{L_t}\kappa_3\boldsymbol{\psi}\boldsymbol{\psi}^{\mathrm{T}}\,dx\end{bmatrix}, \tag{108}$$

$$\mathbf{K}^{\mathrm{ad}}=\begin{bmatrix}\mathbf{0} & -\int_0^{L_t}E_1\frac{\partial\boldsymbol{\phi}}{\partial x}\boldsymbol{\psi}^{\mathrm{T}}\,dx\\ \int_0^{L_t}\boldsymbol{\psi}\frac{\partial\boldsymbol{\phi}^{\mathrm{T}}}{\partial x}\,dx & \int_0^{L_t}\kappa_4\boldsymbol{\psi}\boldsymbol{\psi}^{\mathrm{T}}\,dx\end{bmatrix}, \tag{109}$$

$$\mathbf{G}^{\mathrm{ad}}=\begin{bmatrix}\mathbf{0} & \mathbf{0}\\ \mathbf{0} & -\int_0^{L_t}h\boldsymbol{\psi}\boldsymbol{\psi}^{\mathrm{T}}\,dx\end{bmatrix}, \tag{110}$$

$$\mathbf{R}^{\mathrm{ad}}=\begin{bmatrix}-\boldsymbol{\phi}(0)[u(0,t)-u_m(0,t)]\\ \mathbf{0}\end{bmatrix}, \tag{111}$$

$$\mathbf{d}^{\mathrm{ad}}=\begin{bmatrix}\boldsymbol{\lambda}_u\\ \boldsymbol{\lambda}_\sigma\end{bmatrix},\quad \overline{\mathbf{d}}^{\mathrm{ad}}=\begin{bmatrix}\overline{\boldsymbol{\lambda}}_u\\ \overline{\boldsymbol{\lambda}}_\sigma\end{bmatrix}, \tag{112}$$

where the superscript 'ad' stands for the *adjoint problem*. In (106), $\mathbf{M}^{\mathrm{ad}}$, $\mathbf{C}^{\mathrm{ad}}$, and $\mathbf{K}^{\mathrm{ad}}$ represent the mass-like, damping-like, and stiffness-like matrices of the adjoint semi-discrete equations, respectively. $\mathbf{d}^{\mathrm{ad}}$ is a vector of nodal unknowns comprising nodal values of λ_u and λ_σ. $\overline{\boldsymbol{\lambda}}_u$ is a vector of nodal values representing the temporal integration of λ_u ($\overline{\lambda}_u=\int_0^t\lambda_u(x,z)\,dz$), defined similarly as in (85) for $\overline{\lambda}_\sigma$. $\overline{\mathbf{d}}^{\mathrm{ad}}$ consists of $\overline{\boldsymbol{\lambda}}_u$ and $\overline{\boldsymbol{\lambda}}_\sigma$, and is accommodated by $\mathbf{G}^{\mathrm{ad}}$ in the semi-discrete equations (106). We use a third-order time integration scheme [64] to implement the semi-discrete form (106) of the final-value adjoint problem. We remark that all adjoint-problem matrices can be constructed from their state-problem counterparts, since

$$\mathbf{M}^{\mathrm{ad}}_{ij}=(\mathbf{M}^{\mathrm{st}}_{ji})^{\mathrm{T}},\quad i=1,2,\ j=1,2,$$

$$\mathbf{C}^{\mathrm{ad}}_{ij}=-(\mathbf{C}^{\mathrm{st}}_{ji})^{\mathrm{T}},\quad i=1,2,\ j=1,2,$$

$$\mathbf{K}^{\mathrm{ad}}_{ij}=(\mathbf{K}^{\mathrm{st}}_{ji})^{\mathrm{T}},\quad i=1,2,\ j=1,2,$$

$$\mathbf{G}_{ij}^{ad} = -(\mathbf{G}_{ji}^{st})^{T}, \quad i=1,2,\ j=1,2. \tag{113}$$

6.2.8. The inversion process: reduced-space method

The stationarity of the Lagrangian functional (78) requires solving the coupled state, adjoint, and control problems. Whereas all three problems could be solved simultaneously, here we opt for a reduced-space method, whereby the state problem ((70)–(72)) is solved first for the state variables u and σ with given material property profiles $E_1(x)$ and $E_2(x)$. By doing so, the first optimality condition is satisfied. Then, we solve the adjoint problem ((81)–(83)) using the state solutions computed in the previous step, to obtain the adjoint variables λ_u and λ_σ that satisfy the second optimality condition. As a last step, the material properties $E_1(x)$ and $E_2(x)$ are updated in order for the control equation to be satisfied, using the reduced gradients (89) and (90), respectively. We use a conjugate gradient method with an inexact line search to iteratively update $E_1(x)$ and $E_2(x)$ using the most recent state and adjoint solutions. Details of the optimization process are discussed in [64], and escape the scope of this paper.

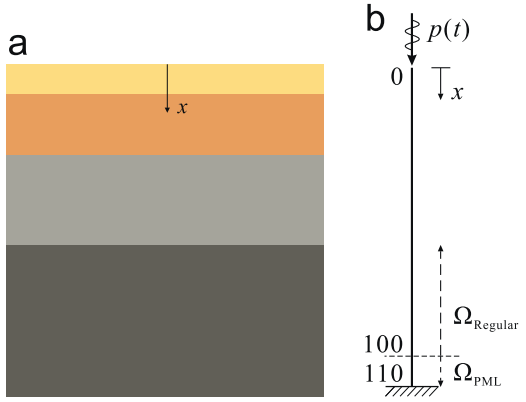

Fig. 15. (a) Heterogeneous semi-infinite soil medium with four horizontal layers; (b) schematic of a one-dimensional PML-truncated domain.

6.3. Numerical results

We consider first a heterogeneous semi-infinite soil medium with four horizontal layers as shown in Fig. 15(a). We model the medium as a one-dimensional PML-truncated domain, with the regular domain occupying $0\ \text{m} \le x < 100\ \text{m}$, and the PML placed at $100\ \text{m} \le x \le 110\ \text{m}$, as shown in Fig. 15(b). We represent the soil's viscoelastic properties using the GMB2. Fig. 16(a) and (b) depicts the target E_1 and E_2 profiles within the PML-truncated domain, respectively. Both profiles have four piecewise constant layers with the same material interface locations. In this setting, the Q factor has four layers as well, owing to (56). Fig. 16(c) represents the target Q factor distribution along the entire domain. The density ρ is $2000\ \text{kg/m}^3$, and a reflection coefficient of $R = 10^{-4}$ is imposed on the PML.

As a source for the inversion, we apply a Gaussian pulse-type load with $f_{max} = 9$ Hz on the surface ($x=0$) as depicted in Fig. 15. Fig. 17 shows the time history and the frequency spectrum of the excitation, respectively. Within this frequency range, the relaxation time parameters τ_1 and τ_2 are approximately constant at 0.45 and 0.02, respectively. For the solution of all viscoelastic inverse medium problems, we used a quadratic–quadratic pair of basis functions for

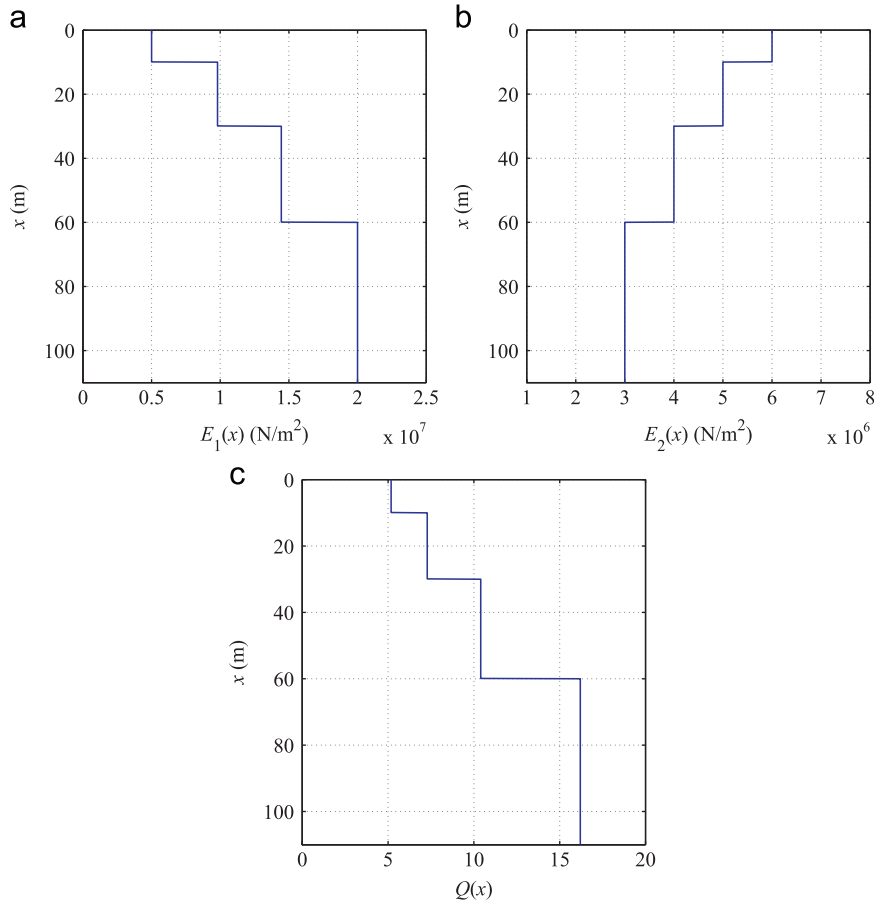

Fig. 16. Target profiles for E_1, E_2, and Q factor. (a) $E_1(x)$, (b) $E_2(x)$, (c) $Q(x)$.

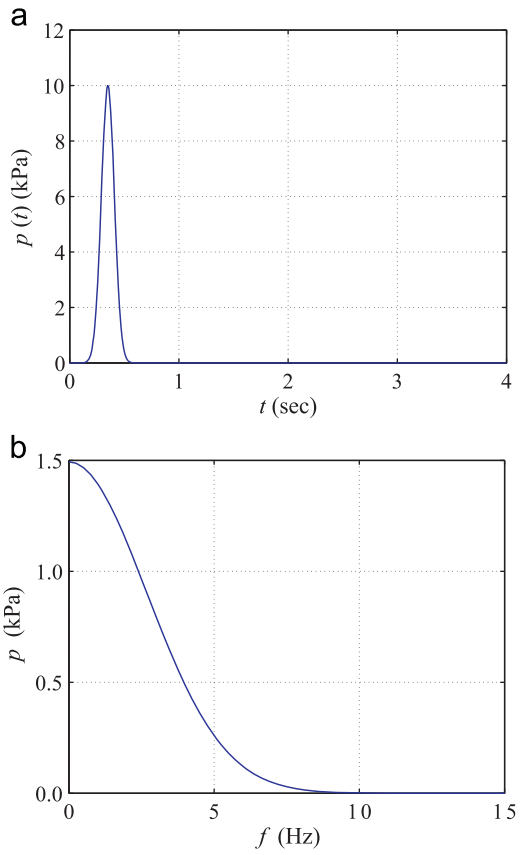

Fig. 17. (a) Time history of the applied stress $p(t)$; $\Delta t = 0.005$ s; (b) frequency spectrum of the applied stress $p(t)$; $f_{max} = 9$ Hz.

the displacement and stress, respectively. We used 110 elements (the element length is 1 m), resulting in a total of 442 unknowns (221 displacement and 221 stress unknowns) associated with each solution of the forward problem. The number of adjoint unknowns is similarly 442, with 221 λ_u and 221 λ_σ unknowns, respectively. We used quadratic approximations for both E_1 and E_2, resulting in a total of 442 inversion variables. We consider three cases for the inversion of viscoelastic parameters. Firstly, we seek to recover the E_1 profile, while assuming that the E_2 profile is *a priori* known. Secondly, the E_2 profile is sought, while the distribution of E_1 is assumed to be known. Finally, we seek to reconstruct both profiles simultaneously, with no *a priori* assumption on both profiles.

6.3.1. *Inverting for E_1 when E_2 (and Q) is fixed*

We are concerned with the reconstruction of the spatial distribution of $E_1(x)$ when $E_2(x)$ is already known. We use the reduced gradient (89) to update E_1. Fig. 18(a) shows the reconstructed E_1 profile (red dots) of the layered soil using TV regularization, when E_2 remains the same as the target. The true profile (blue line) is recovered fairly well. The inversion started with a homogeneous initial guess of $E_1 = 10^7$ N/m^2 (green dots), while a regularization factor continuation scheme [64] was utilized to assist in the convergence of the optimizer. Fig. 18(b) shows the variation of the response misfit with respect to the number of inversion iterations. The misfit reduces to less than 0.0004% of the initial misfit. From these observations, we note that the elastic part ($E_1(x)$) of the GMB2 can be reconstructed well when $E_2(x)$ is previously known.

6.3.2. *Inverting for E_2 (and Q) when E_1 is fixed*

We next turn to the inversion for $E_2(x)$ when $E_1(x)$ is fixed to the target. In this case, we use the reduced gradient (90) to update E_2.

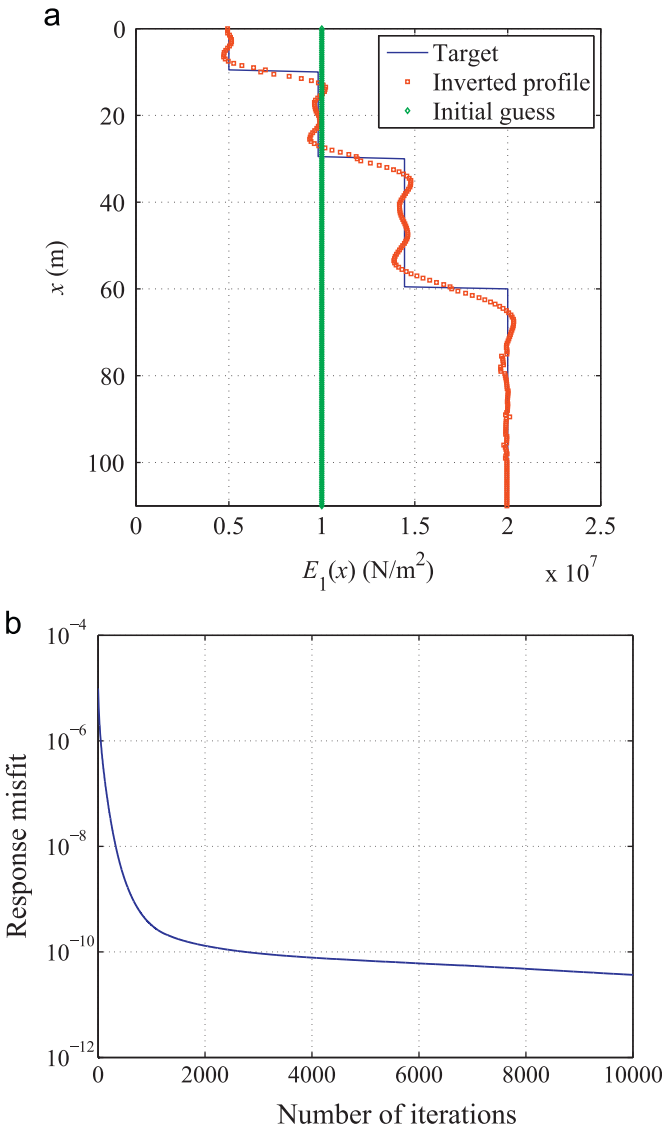

Fig. 18. (a) Initial guess, target, and inverted E_1 profile when E_2 is fixed to the target; (b) response misfit versus number of iterations when inverting for E_1 alone. (For interpretation of the references to color in this figure legend, the reader is referred to the web version of this article.)

We use a homogeneous initial guess of $E_2 = 5 \times 10^6$ N/m^2 (green dots), and recover the target profile using TN regularization. In Fig. 19(a), the E_2 profile is reconstructed (red dots) fairly well, when E_1 remains the same as the target. Fig. 19(b) shows the Q factor profile recovered using (56), as well as the reconstructed E_2 profile. From these results, we note that the damping-related modulus ($E_2(x)$) of the viscoelastic soil medium can be recovered quite well provided that the elastic property ($E_1(x)$) is known in advance. The final misfit is 0.21% of the initial misfit, as shown in Fig. 20.

6.3.3. *Simultaneous inversion for E_1 and E_2 (and Q)*

Next, we attempt to recover both the $E_1(x)$ and $E_2(x)$ profiles when there is no *a priori* information on either of the profiles. This problem entails the reconstruction of both elastic and attenuation parameters ((E_1, E_2) or (E_1, Q)) of the GMB2, given the same surficial measurements as in the case of the single variable inversion. To this end, we use both of the reduced gradients (89) and (90) to update E_1 and E_2, respectively. A difficulty in this problem is that the solution multiplicity issue becomes exacerbated due to the presence of dual inversion variables. To avoid having the optimizer trapped within

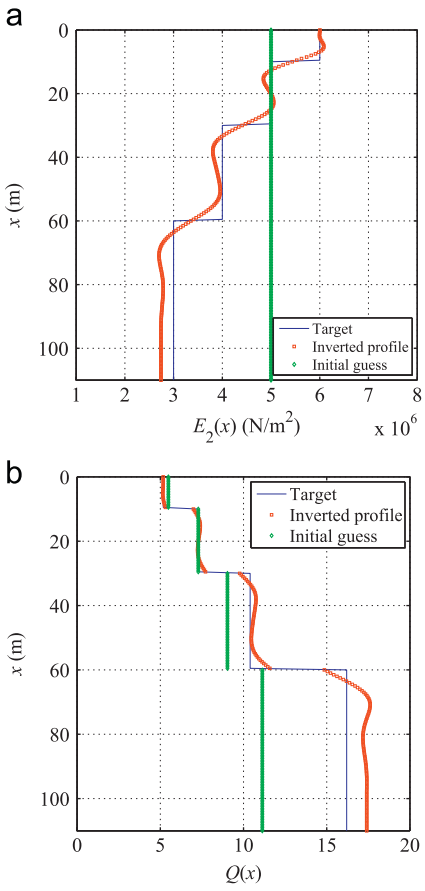

Fig. 19. (a) Target, initial guess, and inverted E_2 profiles, while E_1 is fixed to the target; (b) reconstructed Q factor profile when inverting for E_2 alone. (For interpretation of the references to color in this figure legend, the reader is referred to the web version of this article.)

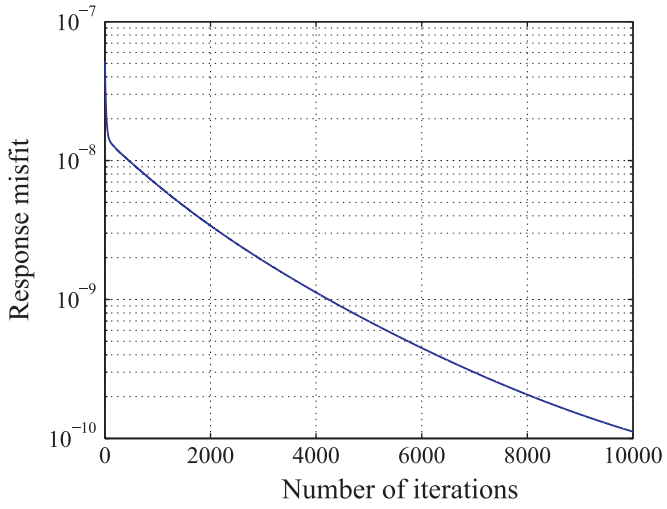

Fig. 20. Response misfit versus number of iterations when inverting for E_2 alone.

the basin of attraction of undesirable local minima, initial guesses and regularization factors should be carefully chosen for both inversion parameters, but there is, in general, no robust systematic way for making these choices.

First, we consider two-parameter inversion for a constant target profile $E_1(x) = 10^7$ N/m^2, and the 4-layer target profile $E_2(x)$ depicted in Fig. 15(b). Fig. 21 shows the target, initial guess, and inverted profiles for $E_1(x)$ and $E_2(x)$, respectively. As shown in the figure, $E_1(x)$

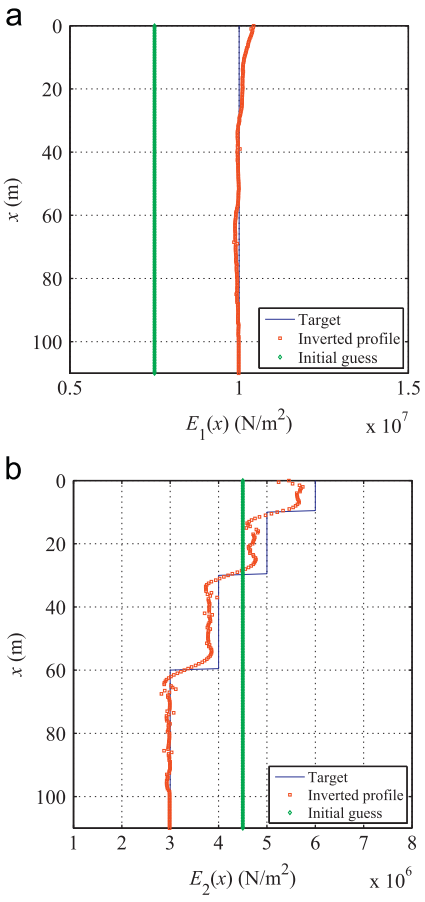

Fig. 21. Target, initial guess, and inverted profiles for E_1 and E_2, respectively. (a) $E_1(x)$, (b) $E_2(x)$.

is well reconstructed, while $E_2(x)$ has moderately well recovered the thickness, location, and material property values of each layer. We used homogeneous initial guesses of $E_1 = 7.5 \times 10^6$ N/m^2 and $E_2 = 4.5 \times 10^6$ N/m^2, and then updated E_1 and E_2 simultaneously at every inversion iteration with the aid of a regularization factor continuation scheme. Fig. 22(a) shows the recovered Q factor profile obtained from the inverted E_1 and E_2 results: Q is remarkably well-reconstructed. As seen in Fig. 22(b), the response misfit reduces to less than 0.00003% of the initial misfit, while three different step lengths have been taken during the entire inversion process.

Next, we attempt the simultaneous two-parameter inversion when both profiles are layered. In particular, we attempt to recover the layered profiles $E_1(x)$ and $E_2(x)$ depicted in Fig. 16. In this case, simultaneously inverting for both properties during every inversion iteration could not lead to satisfactory reconstruction of the target profiles, regardless of the choice of initial guesses, step lengths, and regularization factors. To overcome this difficulty, we use a *staggered* inversion approach, where single variable inversion is followed by simultaneous inversion with a source frequency continuation scheme. In this example, the details are as follows:

- We use constant and linear initial guesses for $E_1(x)$ and $E_2(x)$, respectively. The initial profiles we used are

$$E_1(x) = 10^7 \text{ N/m}^2 \quad \text{for } x \in \Omega_{\text{Regular}}, \tag{114}$$

$$E_2(x) = (-0.035x + 5.3) \times 10^6 \text{ N/m}^2 \quad \text{for } x \in \Omega_{\text{Regular}}. \tag{115}$$

Then, we fix the initial guess of $E_2(x)$ and invert only for $E_1(x)$ using the Gaussian pulse load with $f_{\max} = 9$ Hz shown in Fig. 16.

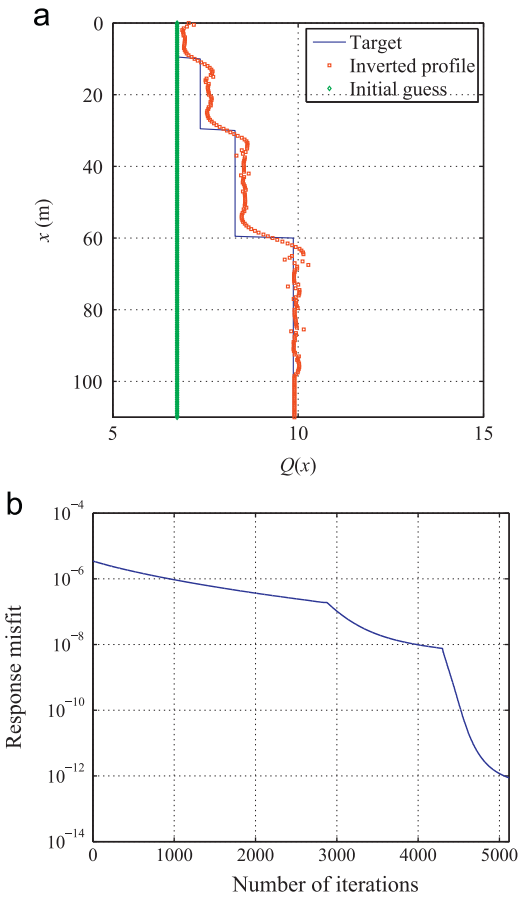

Fig. 22. (a) Inverted Q factor profile and (b) response misfit versus iteration numbers in the simultaneous inversion; E_1 is constant and E_2 has four layers.

- With the updated $E_1(x)$ and the initial guess of $E_2(x)$, we attempt simultaneous inversion using a higher frequency load. In this example, a Gaussian load with $f_{max} = 30$ Hz has been used for the simultaneous inversion.

Fig. 23 shows the results of the two-parameter inversion implemented by the above staggered inversion procedure. As can be seen in the figure, the inverted $E_1(x)$ captures the target quite well, while $E_2(x)$ has some limitations. The inaccurate recovery pattern near the interfaces of $E_2(x)$ is not what we observed in the case of the single variable inversion for $E_2(x)$ (Fig. 19a), where E_2 was recovered well even at the sharp interfaces. However, the variation of the layers can be observed, with the value of E_2 matching closely the target around the middle of each layer. Fig. 24 shows the Q factor profile constructed from the inverted $E_1(x)$ and $E_2(x)$ profiles. A significant point is that, although the reconstruction of $E_2(x)$ is imperfect near the layer interfaces, the recovered Q factor profile captures the sharply varying interfaces quite well. Fig. 25 shows the variation of the misfit against the iteration numbers for each case of the inversion using different source frequencies; the beneficial effect of the source frequency continuation scheme is evident.

7. Conclusions

In this paper we discussed a systematic methodology for imaging the soil's elastic and attenuating properties. To this end, we first discussed models that account for near frequency-independent modeling of the quality factor Q, and still yield constitutive relations

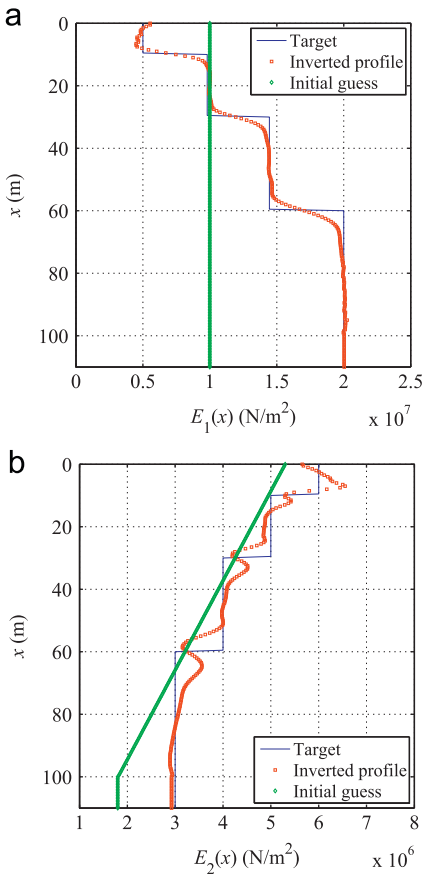

Fig. 23. Target, initial guess, and inverted profiles for E_1 and E_2, respectively; both profiles have four layers. (a) $E_1(x)$, (b) $E_2(x)$.

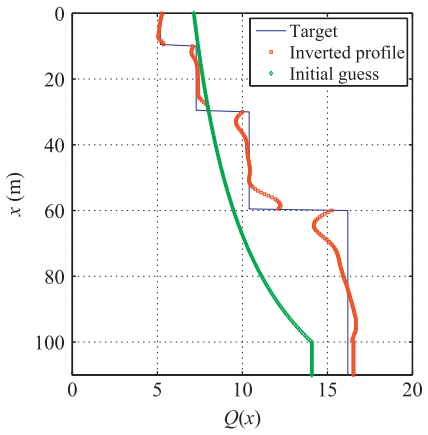

Fig. 24. Target, initial guess, and inverted Q factor profiles when both E_1 and E_2 have four layers.

that can lead to time-domain wave-like equations of computationally manageable complexity. We showed, via forward site analyses, that a relaxed version of the eight-member generalized Maxwell body (the GMB2 model) adequately captures the exact frequency-independent behavior that is supported by the observations. We then incorporated the GMB2 model into a full-waveform-based inversion framework, and deployed regularization and continuation schemes in order to invert simultaneously for the spatially distributed elastic and attenuating properties, when fed only the response of the soil column to probing waves. Our numerical results indicate that, while the elastic properties are well captured, reconstruction of the attenuation profiles is more challenging. Still, very satisfactory

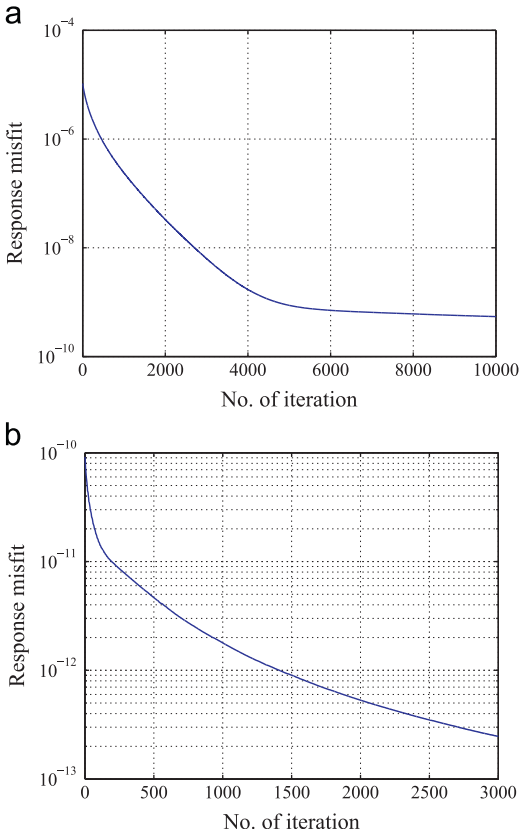

Fig. 25. Response misfit versus iteration numbers in the simultaneous inversion; both E_1 and E_2 have four layers. (a) Single variable inversion with $f_{max}=9$ Hz, (b) simultaneous inversion with $f_{max}=30$ Hz.

results were obtained when a staggered scheme was employed. In summary, the described methodology is directly extensible to problems in higher spatial dimensions, and could lead to the systematic characterization of lossy soils.

Acknowledgments

Partial support for the authors' research has been provided by the National Science Foundation under Grant awards CMMI-0348484 and CMMI-0619078. This support is gratefully acknowledged.

Appendix A

In Section 6, the resulting semi-discrete equation of motion for both the forward and adjoint problems was cast as (e.g., (95))

$$\mathbf{M}\ddot{\mathbf{d}}+\mathbf{C}\dot{\mathbf{d}}+\mathbf{K}\mathbf{d}+\mathbf{G}\overline{\mathbf{d}}=\mathbf{F}, \tag{116}$$

where $\overline{\mathbf{d}}$ is the time-integral of displacements $\mathbf{d}$, i.e.,

$$\overline{\mathbf{d}}=\int_0^t \mathbf{d}(z)\,dz. \tag{117}$$

To integrate (116) in time we use a third-order scheme, extended from the classical Newmark's method. Accordingly, first, the initial conditions are given as

$$\overline{\mathbf{d}}(0)=\overline{\mathbf{d}}_0,\quad \mathbf{d}(0)=\mathbf{d}_0,\quad \dot{\mathbf{d}}(0)=\dot{\mathbf{d}}_0, \tag{118}$$

and the initial accelerations $\ddot{\mathbf{d}}_0$ can then be computed by

$$\ddot{\mathbf{d}}_0=\mathbf{M}^{-1}[\mathbf{F}-\mathbf{C}\dot{\mathbf{d}}_0-\mathbf{K}\mathbf{d}_0-\mathbf{G}\overline{\mathbf{d}}_0]. \tag{119}$$

Use of Taylor series expansions leads to

$$\overline{\mathbf{d}}_{n+1}=\overline{\mathbf{d}}_n+\Delta t\mathbf{d}_n+\frac{\Delta t^2}{2}\dot{\mathbf{d}}_n+\frac{\Delta t^3}{6}\ddot{\mathbf{d}}_\alpha, \tag{120}$$

$$\mathbf{d}_{n+1}=\mathbf{d}_n+\Delta t\dot{\mathbf{d}}_n+\frac{\Delta t^2}{2}\ddot{\mathbf{d}}_\beta, \tag{121}$$

$$\dot{\mathbf{d}}_{n+1}=\dot{\mathbf{d}}_n+\Delta t\ddot{\mathbf{d}}_\gamma, \tag{122}$$

where $\ddot{\mathbf{d}}_\alpha$, $\ddot{\mathbf{d}}_\beta$ and $\ddot{\mathbf{d}}_\gamma$ can be written as

$$\ddot{\mathbf{d}}_\alpha=(1-6\alpha)\ddot{\mathbf{d}}_n+6\alpha\ddot{\mathbf{d}}_{n+1},\quad 0\le\alpha\le\tfrac{1}{6}, \tag{123}$$

$$\ddot{\mathbf{d}}_\beta=(1-2\beta)\ddot{\mathbf{d}}_n+2\beta\ddot{\mathbf{d}}_{n+1},\quad 0\le\beta\le\tfrac{1}{2}, \tag{124}$$

$$\ddot{\mathbf{d}}_\gamma=(1-\gamma)\ddot{\mathbf{d}}_n+\gamma\ddot{\mathbf{d}}_{n+1},\quad 0\le\gamma\le 1. \tag{125}$$

Substituting (123)–(125) into (120)–(122), respectively, results in

$$\overline{\mathbf{d}}_{n+1}=\overline{\mathbf{d}}_n+\Delta t\mathbf{d}_n+\frac{\Delta t^2}{2}\dot{\mathbf{d}}_n+\frac{\Delta t^3}{6}[(1-6\alpha)\ddot{\mathbf{d}}_n+6\alpha\ddot{\mathbf{d}}_{n+1}], \tag{126}$$

$$\mathbf{d}_{n+1}=\mathbf{d}_n+\Delta t\dot{\mathbf{d}}_n+\frac{\Delta t^2}{2}[(1-2\beta)\ddot{\mathbf{d}}_n+2\beta\ddot{\mathbf{d}}_{n+1}], \tag{127}$$

$$\dot{\mathbf{d}}_{n+1}=\dot{\mathbf{d}}_n+\Delta t[(1-\gamma)\ddot{\mathbf{d}}_n+\gamma\ddot{\mathbf{d}}_{n+1}]. \tag{128}$$

After introducing (126)–(128) in the equation of motion at the $(n+1)$th time, there results the following linear system of equations:

$$\mathbf{K}_{\text{eff}}\ddot{\mathbf{d}}_{n+1}=[\mathbf{F}_{\text{eff}}]_{n+1}, \tag{129}$$

where the effective stiffness matrix and load vector $\mathbf{K}_{\text{eff}}$ and $[\mathbf{F}_{\text{eff}}]_{n+1}$, respectively, are

$$\mathbf{K}_{\text{eff}}=\mathbf{M}+\gamma\Delta t\mathbf{C}+\beta\Delta t^2\mathbf{K}+\alpha\Delta t^3\mathbf{G}, \tag{130}$$

$$\begin{aligned}[\mathbf{F}_{\text{eff}}]_{n+1}=\mathbf{F}_{n+1}&-\mathbf{C}[\dot{\mathbf{d}}_n+(1-\gamma)\Delta t\ddot{\mathbf{d}}_n]\\&-\mathbf{K}\left[\mathbf{d}_n+\Delta t\dot{\mathbf{d}}_n+\frac{1-2\beta}{2}\Delta t^2\ddot{\mathbf{d}}_n\right]\\&-\mathbf{G}\left[\overline{\mathbf{d}}_n+\Delta t\mathbf{d}_n+\frac{\Delta t^2}{2}\dot{\mathbf{d}}_n+\frac{1-6\alpha}{6}\Delta t^3\ddot{\mathbf{d}}_n\right].\end{aligned} \tag{131}$$

Once $\ddot{\mathbf{d}}_{n+1}$ is obtained from (129), $\dot{\mathbf{d}}_{n+1}$, $\mathbf{d}_{n+1}$, and $\overline{\mathbf{d}}_{n+1}$ can be computed using (126)–(128). For an average acceleration scheme, (α,β,γ) reduce to $(\frac{1}{12},\frac{1}{4},\frac{1}{2})$, whereas for a linear acceleration scheme, (α,β,γ) reduce to $(\frac{1}{24},\frac{1}{6},\frac{1}{2})$. Numerical damping, though not necessary for the problem at hand, can also be introduced through small perturbations of the parameters α, β, and γ, as customarily done in second-order problems.

References

[1] Johnston DH, Toksöz MN, Timur A. Attenuation of seismic waves in dry and saturated rocks: II. Mechanisms. Geophysics 1979;44(4):691–711.
[2] Tatsuoka F, Uchimura T, Hayano K, Di Benedetto H, Koseki J, Siddiquee MSA. Time-dependent deformation characteristics of stiff geomaterials in engineering practice. In: Jamiolkowski et al., editors. Proceedings of the second international conference of pre-failure deformation characteristics of geomaterials, vol. 2, Torino, Balkema, 2001. p. 1161–262.
[3] Askan A, Akcelik V, Bielak J, Ghattas O. Full waveform inversion for seismic velocity and anelastic losses in heterogeneous structures. Bulletin of the Seismological Society of America 2007;97(6):1990–2008.
[4] Woods RD. Laboratory measurement of dynamic soil properties. American Society of Testing and Materials, ASTM Special Technical Publication STP 1213, 1994. p. 165–90.
[5] Ni SH. Dynamic properties of sand under true triaxial stress states from resonant column/torsional shear tests. Doctoral Dissertation, The University of Texas at Austin, Austin, TX, USA, 1987.
[6] Stokoe KH, Darendeli MB, Andrus RD, Brown LT. Dynamic soil properties: laboratory, field and correlation studies. In: Proceedings of 2nd international conference on earthquake geotechnical engineering, Lisbon, Portugal, 21–25 June, Portuguese Geotechnical Society, Porto, Portugal. Theme Lecture, vol. 3, 1999. p. 811–45.

[7] Knopoff L. Q. Review of Geophysics 1964;2(4):625–60.
[8] Jackson DD, Anderson DL. Physical mechanisms of seismic-wave attenuation. Review of Geophysics 1970;8(1):1–63.
[9] Dziewonski AM. On regional differences in dispersion of mantle Rayleigh waves. Geophysical Journal of Royal Astronomical Society 1971;22:289–325.
[10] Aki K, Richards PG. Quantitative seismology. second ed. Sausalito, CA: University Science Books; 2002.
[11] Iwasaki T, Tatsuoka F, Tokida K, Yasuda S. A practical method for assessing soil liquefaction potential based on case studies at various sites in Japan. In: Proceedings of 2nd international conference on microzonation for safer construction, research and application, vol. 2, San Francisco, CA, 1978. p. 885–96.
[12] Isenhower WM. Torsional simple shear/resonant column properties of San Francisco Bay mud. Master of Science Thesis, The University of Texas at Austin, TX, USA, 1979.
[13] Tatsuoka F, Shibuya S. Deformation characteristics of soil and rocks from field and laboratory test. Report of the Institute of Industrial Science, vol. 1(37), The University of Tokyo, 1992. p. 235.
[14] Kim Y-S, Tatsuoka F, Ochi K. Deformation characteristics at small strains of sedimentary soft rock by triaxial compression tests. Geotechnique 1994;44(3):461–78.
[15] Fioravante V, Jamiolkowski M, Lo Presti DCF. Stiffness of carbonatic quiou sand. In: Proceedings of the XIII ICSMFE, vol. 1, New Delhi, India, 1994. p. 163–7.
[16] Porovic E, Jardine RJ. Some observations on the static and dynamic shear stiffness of Ham River Sand. In: Proceedings of international symposium on pre-failure deformation of geomaterials, vol. 1, IS-Hokkaido, Balkema, 1994. p. 25–30.
[17] Tatsuoka F, Sato T, Park C-S, Kim Y-S, Mukabi JN, Kohata Y. Measurement of elastic properties of geomaterials in laboratory compression test. ASTM Geotechnical Testing Journal 1994;17(1):80–94.
[18] Tatsuoka F, Lo Presti DCF, Kohata Y. Deformation characteristics of soils and soft rocks under monotonic and cyclic loads and their relationships. In: III International conference on recent advances in geotechnical earthquake engineering and soil dynamics. University of Missouri-Rolla, St. Louis, MO, 1995.
[19] d'Onofrio A, Santucci de Magistris F, Silvestri F, Vinale F. Behaviour of compacted sand-bentonite mixtures from small to medium strains. In: Proceedings of first earthquake geotechnical engineering conference, vol. 1, Tokyo, Balkema, 1995. p. 133–8.
[20] d'Onofrio A, Silvestri F, Vinale F. Strain rate dependent behavior of a natural stiff clay. Soils and Foundations 1999;39(2):69–82.
[21] Di Benedetto H, Tatsuoka F. Small strain behavior of geomaterials: modeling of strain rate effects. Soils and Foundations 1997;37(2):127–38.
[22] Vucetic M, Tabata K. Influence of soil type on the effect of strain rate on small-strain cyclic shear modulus. Soils and Foundations 2003;43(5):161–73.
[23] Hardin B, Black W. Sand stiffness under various triaxial stresses. Journal of the Soil Mechanics and Foundations Division, ASCE 1966;92(2):27–42.
[24] Bolton MD, Wilson JMR. An experimental and theoretical comparison between static and dynamic torsional soil tests. Geotechnique 1989;39(4):585–99.
[25] Kim DS. Deformation characteristics of soils at small to intermediate strains from cyclic tests. Doctoral Dissertation, The University of Texas at Austin, TX, USA, 1991.
[26] Wang YH, Santamarina JC. Attenuation in sand an exploratory study on the small-strain behavior and the influence of moisture condensation. Granular Matter 2007;9(6):365–76.
[27] Shibuya S, Mitachi T, Fukuda F, Degoshi T. Strain rate effects on shear modulus and damping of normally consolidated clay. ASTM Geotechnical Testing Journal 1995;18(3):365–75.
[28] Papa V, Silvestri F, Vinale F. Analisi delle propiet di un tipico terreno piroclastico mediante prove di taglio semplice. Atti del Convegno Nazionale del Coordinamento per gli Studi di Ingegneria Geotecnica, Monselice (PD), 1988.
[29] Tatsuoka F, Kohata Y. Stiffness of hard soils and soft rocks in engineering applications. Report of the Institute of Industrial Science, The University of Tokyo, vol. 38(5), 1995. p. 235.
[30] Stokoe II KH, Hwang SK, Lee JNK, Andrus RD. Effects of various parameters on the stiffness and damping of soils at small to medium strains, vol. 2, IS Hokkaido, Balkema, 1995. p. 785–816.
[31] Lo Presti DCF, Pallara O, Cavallaro A. Damping ration of soils from laboratory and in-situ tests. In: Proceedings of XIV ICSMFE, seismic behavior of ground and geotechnical structures, Balkema, Rotterdam, 1997. p. 391–400.
[32] Cavallaro A, Lo Presti DCF, Maugeri M, Pallara O. Strain rate effect on stiffness and damping of clays. Italian Geotechnical Review 1998;XXXII(4):30–49.
[33] Leroueil S, Marques MES. Importance of strain rate and temperature effects in geotechnical engineering: measuring and modeling time dependent soil behavior. GSP, vol. 61. New York: ASCE; 1996. p. 1–60.
[34] Krönig RL. On the theory of dispersion of x-rays. Journal of the Optical Society of America and Review of Scientific Instruments 1926;12:547–57.
[35] Kolsky H. The propagation of stress pulses in viscoelastic solids. Philosophical Magazine Series 8 1956;I(8):693–710.
[36] Wang Y, Guo J. Modified Kolsky model for seismic attenuation and dispersion. Journal of Geophysics and Engineering 2004;1:187–96.
[37] Futterman WI. Dispersive body waves. Journal of Geophysical Research 1962;67(13):5279–91.
[38] Strick E. The determination of Q, dynamic viscosity and transient creep curves from wave propagation measurements. Geophysical Journal of the Royal Astronomical Society 1967;13:197–218.
[39] Kjartansson E. Constant Q wave propagation and attenuation. Journal of Geophysical Research 1979;84(B9):4737–48.
[40] Azimi SHA, Kalinin AV, Kalinin VV, Pivovarov BL. Impulse and transient characteristics of media with linear and quadratic absorption laws. Izvestiya Earth Physics 1968;2:42–54.
[41] Müller G. Rheological properties and velocity dispersion of a medium with power-law dependence of Q on frequency. Journal of Geophysics 1983;54: 20–9.
[42] Cole KS, Cole RH. Dispersion and absorption in dielectrics: I. Alternating current characteristics. The Journal of Chemical Physics 1941;9:341–51.
[43] Maxwell JC. On the dynamical theory of gases. Philosophical Magazine 1868;33:129–45.
[44] Thompson W. On the elasticity and viscosity of metals. Proceedings of the Royal Society of London A 1865;14:289–97.
[45] Fung H-C, Tong P. Classical and computational solid mechanics. In: Advanced series in engineering science, vol. 1. World Scientific Publishing Co.; 2001.
[46] Semblat J-F. Rheological interpretation of Rayleigh damping. Journal of Sound and Vibration 1997;206(5):741–4.
[47] Liu H-P, Anderson DL, Kanamori H. Velocity dispersion due to anelasticity: implications for seismology and mantle composition. Geophysical Journal of the Royal Astronomical Society 1976;47:41.
[48] Bourbie T, Coussy O, Zinzner B. Acoustics of porous media. Gulf Publishing Company; 1987.
[49] Lucet N. Vitesse et attenuation des ondes elastiques soniques et ultrasoniques dans les roches sous pression de confinement. Doctoral Dissertation, University Paris VI, France, 1989.
[50] Semblat JF. Amortissement et dispersion des ondes: points de vue physique et numerique. Revue Francaise de Genie Civil 1998;2(1):91–111.
[51] Day SM, Minster JR. Numerical simulation of attenuated wavefields using a Pade approximant method. Geophysical Journal of the Royal Astronomical Society 1984;78:105–18.
[52] Day SM. Efficient simulation of constant Q using coarse-grained memory variables. Bulletin of the Seismological Society of America 1998;88:1051–62.
[53] Ma S, Liu P-C. Modeling of the perfectly matched layer absorbing boundaries and intrinsic attenuation in explicit finite-element methods. Bulletin of the Seismological Society of America 2006;96(5):1779–94.
[54] Emmerich H, Korn M. Incorporation of attenuation into time-domain computations of seismic wave fields. Geophysics 1987;52:1252–64.
[55] Carcione JM, Kosloff D, Kosloff R. Wave propagation simulation in a linear viscoacoustic medium. Geophysical Journal of the Royal Astronomical Society 1988;93:393–407.
[56] Carcione JM, Kosloff D, Kosloff R. Viscoacoustic wave propagation simulation in the earth. Geophysics 1988;53:769–77.
[57] Mozco P, Kristek J, Halada L. The finite difference method for seismologists: an introduction (SPICE project). Comenius University, Bratislava, Slovakia, 2004.
[58] Liu P-C, Archuleta RJ. Efficiency modeling of Q for 3D numerical simulation of wave propagation. Bulletin of the Seismological Society of America 2006;96: 1352–8.
[59] O'Connell RJ, Budiansky B. Measures of dissipation in viscoelastic media. Geophysical Research Letters 1978;5:5–8.
[60] Liu P-C, Hartzell S, Stephenson W. Nonlinear multiparametric inversion using a hybrid global search algorithm: applications in reflection seismology. Geophysical Journal International 1995;122:991–1000.
[61] Bardet JP, Tobita T. NERA: a computer program for nonlinear earthquake site response analyses of layered soil deposits. User Manual, University of Southern California, Department of Civil Engineering, 2001.
[62] Hashash YMA, Park D. Viscous damping formulation and high frequency motion propagation in nonlinear site response analysis. Soil Dynamics and Earthquake Engineering 2002;22(7):611–24.
[63] Kang JW, Kallivokas LF. Mixed unsplit-field perfectly-matched-layers for transient simulations of scalar waves in heterogeneous domains. Computational Geosciences 2010;14:623–48.
[64] Kang JW. A mixed unsplit-field PML-based scheme for full waveform inversion in the time-domain using scalar waves. Doctoral Dissertation, The University of Texas at Austin, Austin, TX, USA, 2010.